

Chapter 4

Multi-scale modelling of dry granular flows

4.1 Introduction

In nature, instabilities of slopes or cliffs are dramatic events involving sudden release of a large mass of soil. However, the prediction of catastrophic events still represents challenge, one difficulty being our incomplete understanding of the dynamics of granular flows (Rondon et al., 2011). Understanding the mechanics is of particular importance for risks assessment. Small scale laboratory experiments are usually unable to properly capture the dynamics of geophysical events. However, they can be useful to precisely study physical mechanisms, which may play a role in real flows (Iverson, 1997).

Conventionally, granular materials such as soils are modelled as a continuum. On a macroscopic scale, granular materials exhibit many collective phenomena and the use of continuum mechanics to describe the macroscopic behaviour can be justified. However, on a grain scale, the granular materials exhibit complex solid-like and/or fluid-like behaviour depending on how the grains interact with each other. Numerical studies at grain scale allows a precise understanding of the internal flow structure. Recent works on granular materials suggest that a continuum law may be incapable of revealing in-homogeneities at the grain-scale level, such as orientation of force chains, which are purely due to micro-structural effects Rycroft et al. (2009). Discrete Element approaches are capable of simulating the granular material as a discontinuous system allowing one to probe into local variables such as position, velocities, contact forces, etc. The fundamental question is how to model granular materials which exhibit complex phenomenon. It is important to understand the mechanics of granular flows and the ability and limitations of continuum methods in capturing the flow dynamics.

¹ 4.2 Granular column collapse

² The collapse of a granular column, which mimics the collapse of a cliff, has been extensively
³ studied in the case of dry granular material (Hogg, 2007; Kerswell, 2005; Lajeunesse et al.,
⁴ 2004; Lo et al., 2009; Lube et al., 2005; Staron and Hinch, 2007; Zenit, 2005). The granular
⁵ column collapse experiment involves filling a rectangular channel of height H_0 and width L_0
⁶ with a granular material of mass ‘m’ (see figure 4.1). The granular column is then released
⁷ *en masse* by quickly removing the gate, thus allowing the granular material to collapse onto
⁸ the horizontal surface, forming a deposit having a final height H_f and length L_f . Despite the
⁹ complexity of the intermediate flow dynamics, experimental investigations have shown that the
¹⁰ flow evolution, the spreading velocity, the final extent of the deposit, and the energy dissipation
¹¹ can be scaled in a quantitative way independent of the substrate properties, grain size, density,
¹² and shape of the granular material and released mass (Lajeunesse et al., 2005; Lube et al., 2005;
¹³ Staron and Hinch, 2007). The granular collapse has also been studied using discrete element
¹⁴ method, which allows precise measurement of the internal flow structure (Lo et al., 2009;
¹⁵ Staron and Hinch, 2006, 2007; Utili et al., 2014). Power laws relating the final run-out and
¹⁶ height to the initial aspect ratio of the column were observed. These findings immediately pose
¹⁷ the question: are these simple scaling fortuitous, an oversimplification, or in fact indicative of a
¹⁸ simple dynamical balance?

¹⁹ Granular flows are conventionally modelled as a frictional dissipation process in continuum
²⁰ mechanics but the lack of influence of inter-particle friction on the energy dissipation and
²¹ spreading dynamics (Lube et al., 2005) is surprising. However, Kerswell (2005) showed the run-
²² out behaviour has a clear material dependence, which corroborates the conclusion of Lajeunesse
²³ et al. (2004) and softens that of Lube et al. (2005). The collapse of a granular column on a
²⁴ horizontal surface is a simple case of granular flow, however a proper model that describes
²⁵ the flow dynamics is still lacking. Simple mathematical models based on conservation of
²⁶ horizontal momentum capture the scaling laws of the final deposit, but fail to describe the initial
²⁷ transition regime. From a theoretical point of view, the spreading has been described using
²⁸ depth averaged equations (Kerswell, 2005; Larrieu et al., 2006). The depth-averaged and Saint-
²⁹ Venant equations struggle to recover the precise dynamic behaviour of the system (Warnett
³⁰ et al., 2013) and only succeeds in predicting the scaling observed for aspect ratio less than one.
³¹ However, describing larger aspect ratio and capturing the initial stage of the collapse, when
³² the grains experience a rapid change of direction from vertical to horizontal, remain an open
³³ challenge,

³⁴ In the present study, multi-scale numerical modelling, i.e. grain-scale modelling and
³⁵ continuum analyses, of the quasi-two dimensional collapse of granular columns are performed
³⁶ using Discrete Element (DEM) approach and Generalised Interpolation Material Point Method

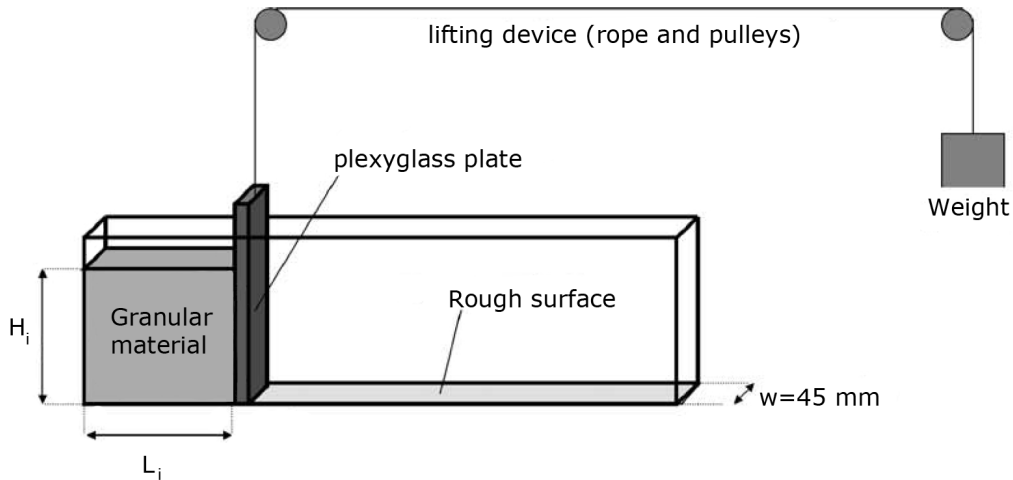


Figure 4.1 Schematic of experimental configuration for 2-D collapse in a rectangular channel, ([Lajeunesse et al., 2004](#))

(GIMPM). GIMPM, a hybrid Eulerian – Lagrangian approach, with Mohr-Coloumb failure criterion is used to describe the continuum behaviour of granular column collapse. While the micro-mechanics of the flow is captured using DEM simulations. Comparing the grain scale behaviour with the continuum simulations highlights the limitations of continuum approaches in modelling the dense granular flows and their ability (or lack thereof) in capturing the complex micro-scale rheology.

4.2.1 Numerical set-up

In this study, numerical simulations of granular columns are analogous to the experimental investigation of column collapse performed by [Lajeunesse et al. \(2004\)](#). The experimental configuration of [Lajeunesse et al. \(2004\)](#) is shown in figure 4.1. Granular material of mass ' M ' was poured into a container to form a rectangular heap of length ' L_0 ', height ' H_0 ' and thickness ' W '. The internal friction angle and the wall friction between the wall and the glass beads measured by [Lajeunesse et al. \(2004\)](#) are listed in table 4.1. The gate was then quickly removed to release the granular mass that spreads in the horizontal channel until it comes to rest. The final run-out distance ' L_f ' and the collapsed height ' H_f ' were measured. The run-out distance and collapse height exhibit a power law relation with the initial aspect ratio ' a ' ($= H_0/L_0$) of the column.

Granular materials when released suddenly on a horizontal surface exhibit transient flow. In this study, the mechanism of flow initiation, spreading dynamics and energy dissipation are studied for varying initial aspect ratios of the granular column. DEM soil grain characteristics match that of the experiment. The particle size distribution (PSD) is one of the most impor-

Table 4.1 Material properties of glass ballotini ([Lajeunesse et al., 2004](#))

Parameter	Value
Mean diameter	1.15 mm
Repose angle	$22 \pm 0.5^\circ$
Avalanche angle	$27.4 \pm 0.5^\circ$
Wall friction angle	$24.8 \pm 0.2^\circ$

tant factors controlling landslide initiation and soil permeability. Cumulative β distribution (described in ??) is used to generate a graded sample with a mean grain diameter of 1.15mm (see figure 4.2b). The DEM sample is composed of ~ 3000 disks with a uniform distribution of diameters by volume fractions in the range $[d_{min}, d_{max}] = 0.92 - 1.38$ mm with polydispersity $r = \frac{d_{max}}{d_{min}} = 1.5$. The granular column is prepared by allowing the randomly placed grains to undergo ballistic deposition with a constant potential head between layers of soil grains. A snapshot of the sample generated is shown in figure 4.2a. A DEM sample with soil grains arranged in a regular hexagonal lattice is also used to study the influence of crystallisation and jamming on the run-out behaviour.

The overlap between grains are determined by the stiffness k_n of the spring in the normal direction. Typically, an average overlap in the range 0.1 to 1.0% is desirable [Zenit \(2005\)](#) and the spring constant is chosen to produce grain overlaps in this range. The stiffness is determined as

$$k_n = \frac{2\pi G}{(1-\nu)[2\ln(\frac{2r}{A}) - 1]} \quad (4.1)$$

$$A = \left[\frac{2r(1-\nu)f_n}{\pi G} \right]^{\frac{1}{2}}, \quad (4.2)$$

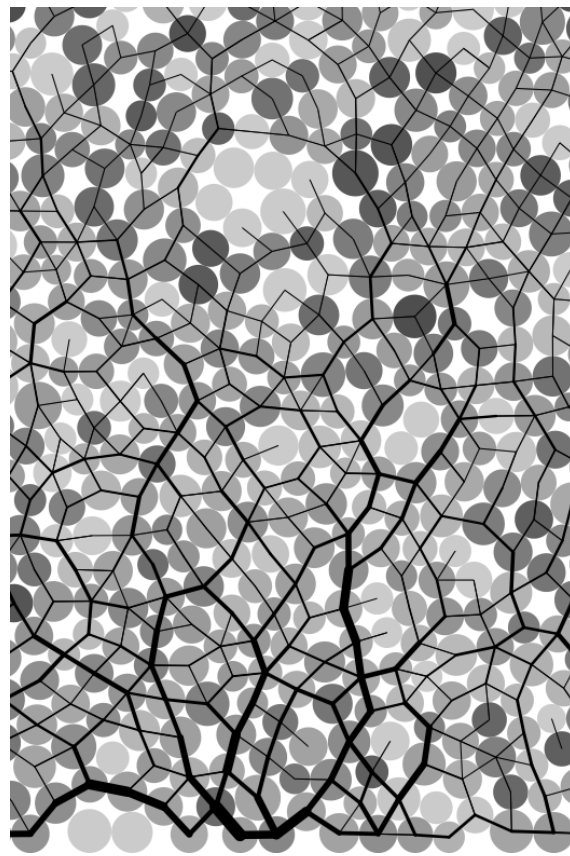
where f_n is the normal contact force; G is the shear modulus; ν is the Poisson's ratio and r is the radius of the grain. A simpler form of stiffness for a spherical grain is defined as

$$k_n = 4ER, \quad (4.3)$$

where E is the Young's modulus of the material and R is the radius of the grain. [Cambou et al. \(2009\)](#) observed that the contact model has negligible influence on the run-out behaviour of rapid granular flows. The granular collapse simulations performed using non-linear Hertz-Mindlin contact model and the linear-elastic contact model showed no significant difference on the granular flow behaviour [Utili et al. \(2014\)](#). Linear-elastic contact model is used in the

4.2 Granular column collapse

5



(a) DEM sample prepared using ballistic deposition

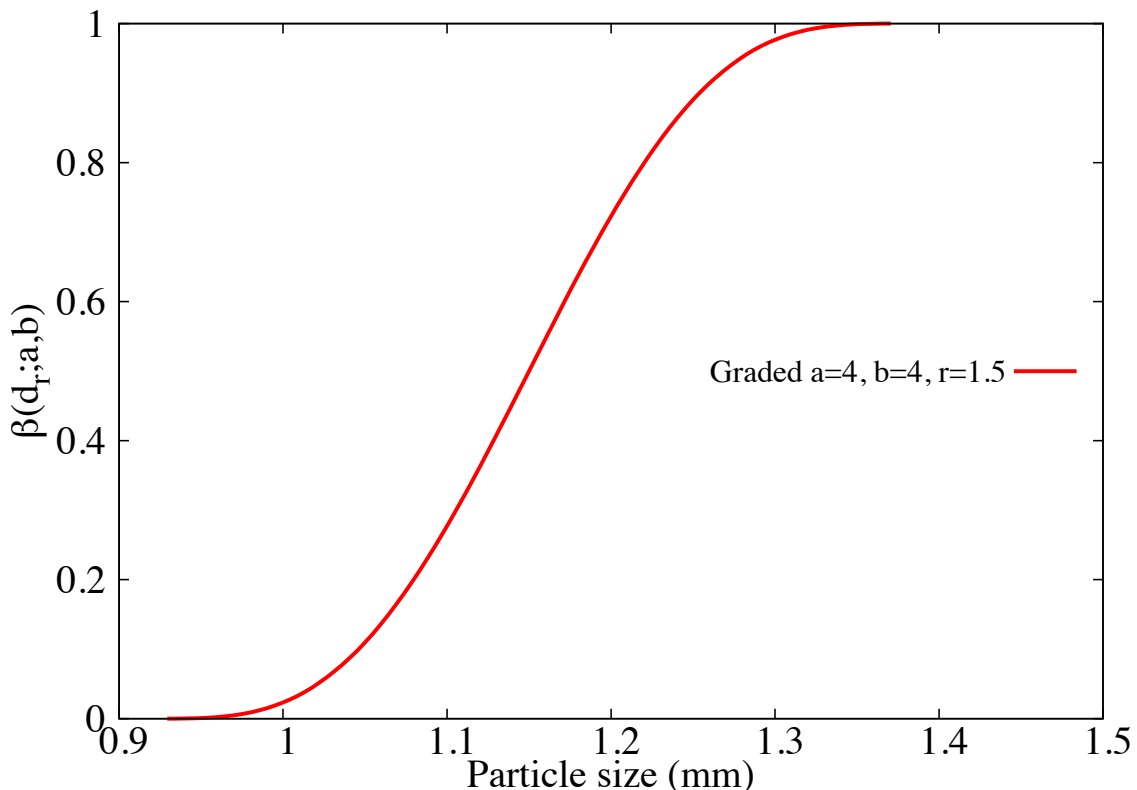
(b) DEM grains generated using the cumulative β distribution

Figure 4.2 DEM sample characteristics

Table 4.2 Micro-mechanical parameters used in DEM simulations

Parameter	Value
Young's modulus of glass bead	$70 \times 10^9 \text{ N m}^{-2}$
Poisson's ratio	0.22 - 0.24
Diameter of glass beads	0.92 to 1.38 mm
Normal and shear stiffness of grains	$1.6 \times 10^8 \text{ N m}^{-1}$
Normal and shear stiffness of wall	$4 \times 10^8 \text{ N m}^{-1}$
Inter-particle friction coefficient, μ	0.53
Wall friction coefficient	0.466
Coefficient of restitution, ϵ	0.755

¹ present study due to its simplicity and lower computation time requirement. The maximum
² tangential force is limited by the Mohr-Coloumb criterion.

³ [Staron and Hinch \(2006\)](#) observed that the coefficient of restitution ϵ was dramatically
⁴ changing the behaviour of the systems for $\epsilon \rightarrow 1$; in particular, this dramatic change is
⁵ expected to become more important for increasing values of a . On the contrary, for $\epsilon \leq 0.8$,
⁶ the influence of the coefficient of restitution becomes negligible. In the present study, a value
⁷ of 0.75 is adopted as the coefficient of restitution, similar values of restitution coefficient
⁸ was adopted by [Girolami et al. \(2012\)](#); [Zenit \(2005\)](#). The normal damping coefficient C_n is
⁹ appropriately chosen to achieve the required coefficient of restitution ϵ :

$$\text{10} \quad C_n = 2\gamma\sqrt{m_{ij}k_n} \quad (4.4)$$

$$\text{11} \quad \text{where } \gamma = -\frac{\ln(\epsilon)}{\sqrt{\pi^2 + \ln^2(\epsilon)}}, \quad \text{and} \quad m_{ij} = \frac{m_i m_j}{m_i + m_j}. \quad (4.5)$$

¹³ The micro-mechanical parameters used in this study are presented in table 4.2. Due to the
¹⁴ unsteady nature of the flow, the grains get dispersed on the horizontal plane as discrete bodies
¹⁵ start to separate from the main mass, hence the run-out distance is calculated as the position of
¹⁶ the farthest grain which has at least one contact with the main mass.

¹⁷ GIMPM with Mohr-Coloumb constitutive model is used to simulate plane strain collapse
¹⁸ of granular columns. [Crosta et al. \(2009\)](#) observed that the Mohr-Coloumb with non-associate
¹⁹ flow rule is able to capture granular collapse dynamics and models the strong vertical motion
²⁰ components, but it does not suffer the limitations of typical shallow water equation methods.
²¹ In order to understand the ability and limitations of continuum approaches in capturing the
²² local rheology, it is important to scale the grain scale properties, such as inter-particle friction
²³ and stiffness, to the continuum scale (macroscopic friction and Young's modulus). [Crosta et al.](#)
²⁴ ([2009](#)) observed that the friction angle plays a significant role on the run-out behaviour. In

4.2 Granular column collapse

7

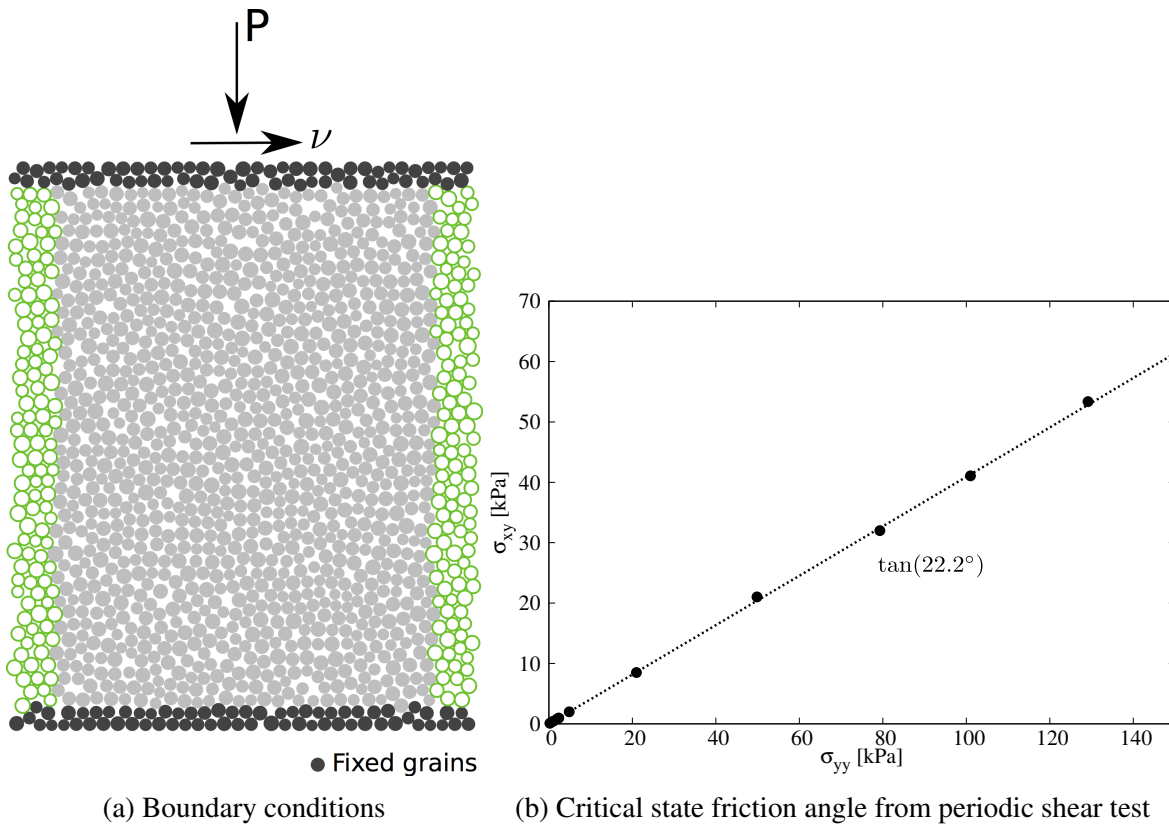


Figure 4.3 Periodic shear test

MPM simulations, the granular flow is assumed to be in critical state and the critical state friction angle is used in the Mohr-Coloumb model. In order to obtain the critical state friction angle of the granular sample, a shear test is performed using 1078 DEM grains. A bi-periodic boundary condition is adopted on the sides of the sample (see figure 4.3a). Two layers of fixed grains (shown in black) is placed at the top and the bottom of the shear sample. A normal pressure ‘P’ and a horizontal velocity ν is applied to the fixed grains at the top of the shear sample. The normal effective stress is varied in the sample and the average shear stress of the sample is measured. The sample was sheared until critical state was reached. The slope of shear stress versus normal effective stress gives the critical state friction angle. A critical state friction angle of 22.2° is obtained. The macroscopic friction angle is in the range observed by Estrada et al. (2008); Mitchell and Soga (2005). The Young’s modulus of the granular assembly is obtained as the initial slope of the stress-strain plot of a uni-axial compression of a granular column using DEM.

Guilkey et al. (2003) suggests using at least four material points per cell for large deformation problems. In the present study, 16 material points per cell is adopted. If the mesh is too fine and the number of particles is too large, the particle size $2l/p$ decreases, and the GIMPM

Table 4.3 Parameters used in continuum simulations

Parameter	Value
Material point spacing	0.575 mm
Number of material points per cell	16
Young's Modulus, E	1.98×10^6 Pa
Poisson's ratio, ν	0.22 to 0.24
Friction angle, ϕ	$23.2 \pm 0.2^\circ$
Dilatancy angle, Φ	0°
Density, ρ	1800 kg m^{-3}
Wall friction	0.466
Time step increment	1.0×10^{-6} s

¹ interpolation function tends to approach the original MPM function, as shown by [Bardenhagen and Kober \(2004\)](#). Hence GIMPM loses the merit that it reduces the numerical noise due to material points crossing the background mesh. In addition, the probability of particles crossing the background mesh increases with decrease in mesh size, hence, more noise can be produced [Abe et al. \(2013\)](#). The effect of number of material points per cell on the run-out behaviour is discussed in section 4.2.9. Each material point represents one-fourth of a DEM soil grain. The parameters used for the continuum analyses are presented in table 4.3.

4.2.2 Deposit morphology

MPM and DEM simulations of granular column collapse are performed by varying the initial aspect ratio of the column. The normalized final run-out distance, $\Delta L = (L_f - L_0)/L_0$, as a function of the initial aspect ratio 'a' of the column is presented in figure 4.4. Similar to the experimental behaviour a power law relation between the run-out and the initial aspect ratio of the column is observed. Two distinct flow regimes can be seen: (a) for 'a' < 1.7 a linear relation between the spread and aspect ratio can be observed, and (b) for 'a' > 1.7 a power-law relationship exists. In the present study, the following scaling law for the run-out (using DEM) is observed:

$$\frac{L_f - L_0}{L_0} \approx \begin{cases} 1.67a, & a \lesssim 2.3 \\ 2.5a^{2/3}, & a \gtrsim 2.3 \end{cases} \quad (4.6)$$

Both, MPM and DEM simulations are able to capture the linear relationship for 'a' < 1.7, and the simulation results agree with the experimental investigation [Lajeunesse et al. \(2005\)](#). This shows that a simple frictional dissipation model is able to capture the flow dynamics for

columns with smaller aspect ratio. For ‘a’ < 1.7, the normalised run-out distance predicted using DEM simulations are very close to the run-out observed in the experiments. DEM simulations with hexagonal packing shows shorter run-out distances in comparison to randomly packed sample. This difference in the run-out behaviour might be due to the crystallisation and jamming effects in hexagonal packing. The small difference in the final run-out between DEM and experimental results can be attributed to the variation in the packing of grains. Also, the experimental data corresponds to granular column collapse in a rectangular channel, the collapse is not a pure two-dimensional collapse as in the case of numerical simulations.

Significant difference in the final run-out between MPM, which is based on a simple frictional model for dissipation of potential energy, and DEM simulations for ‘a’ > 1.7 indicates a change in the mechanism of energy dissipation for columns with large aspect ratios (‘a’ > 1.7). [Staron and Hinch \(2005\)](#) observed that a constant frictional dissipation model cannot describe a power-law relation observed at large aspect ratio. A transition in the run-out behaviour at an aspect ratio of 1.7 indicates a change in flow dynamics. Similar behaviour in the run-out distance was observed by [Bandara \(2013\)](#) for columns with large the aspect ratio ≥ 2 .

The longer run-out distance in MPM simulations at large aspect ratios might be influenced by the amount of material mobilised during the collapse. In tall columns, the entire column participates in the flow, in contrast to short columns where the collapse is due to avalanching of flanks, [Lajeunesse et al. \(2004\)](#). It is possible that MPM simulations collapses more resulting in longer run-out distance. Figure 4.5 shows the normalized final height as a function of the initial aspect ratio of the column. Similar to the run-out behaviour, the normalised-height also shows two distinct regimes. The scaling of final height of the column with the initial aspect ratio of the column can be written as

$$\frac{H_f}{L_i} \propto \begin{cases} a, & a \lesssim 0.7 \\ a^{2/3}, & a \gtrsim 0.7 \end{cases} \quad (4.7)$$

The final height predicted by both DEM and MPM simulations match the experimental data for columns with smaller aspect ratio (‘a’ ≤ 0.7). Linear relationship between the final height and the aspect ratio indicates that only a part of the granular column is mobilised during the collapse. For tall columns, both approaches predict similar normalised height. However, the normalised height observed in MPM is higher than in DEM simulations, which is in contrast to the idea of increase in the amount of material mobilised during the collapse in MPM simulations resulting in longer run-out distance. Hence, the longer run-out observed in MPM simulations is due a change in the flow dynamics at higher aspect ratios, which is not captured in MPM simulations. The final height of a column is controlled by the amount of static region in the

1 granular column collapse, while the run-out distance is essentially a function of the flowing
 2 mass. Hence, it is essential to compare the evolution of flow and the internal flow structure in
 3 DEM and MPM simulations.

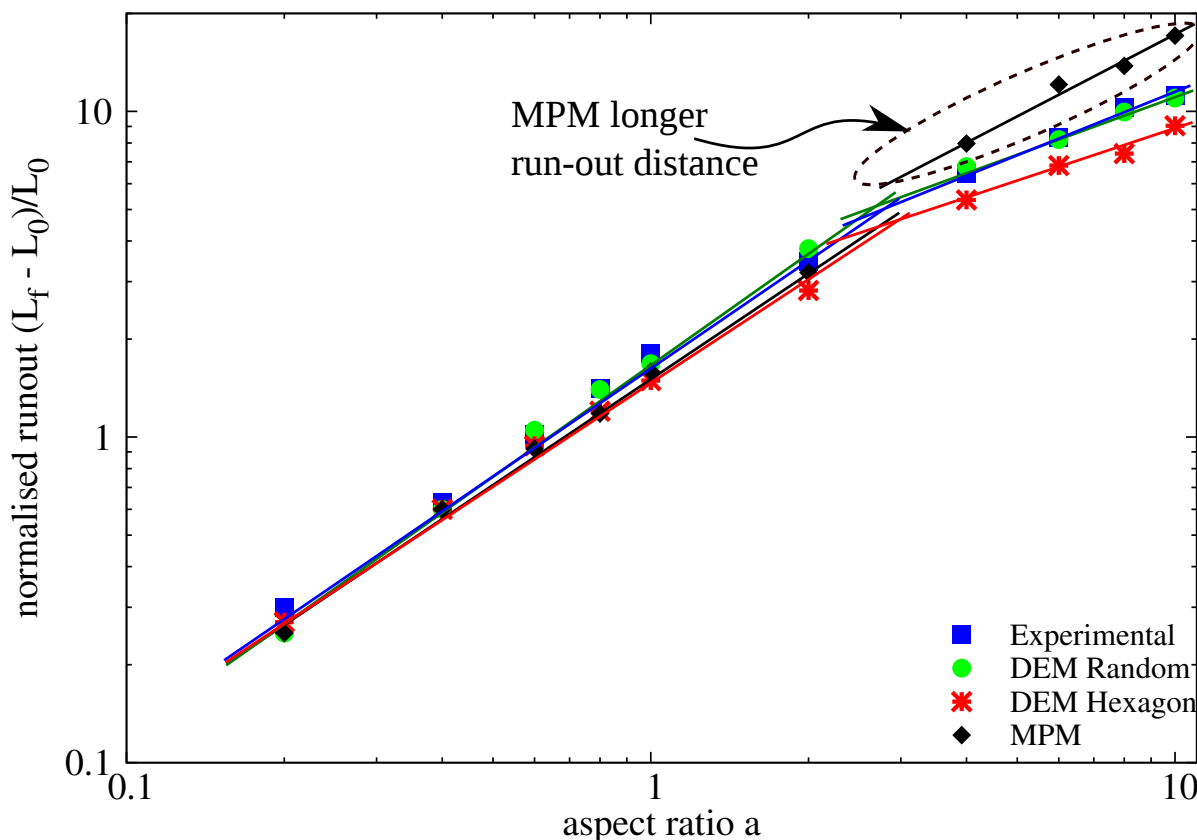


Figure 4.4 Normalised final run-out distance for columns with different initial aspect ratio

4.2.3 Flow evolution and internal flow structure

5 The normalised run-out and height as a function of the aspect ratio indicates that, for a given
 6 granular material and substrate properties, the flow dynamics and the final deposit morphology
 7 are independent of the volume of granular material released, but depend only on the geometry
 8 of the column. A power law relationship is observed between the run-out distance and the
 9 initial aspect ratio of the column. A transition in the run-out behaviour at an aspect ratio of 2.3
 10 indicates a change in the flow dynamics.

11 For smaller aspect columns ('a' < 2.3), the flow is initiated by a failure at the edge of the
 12 pile along a well-defined fracture surface. The granular mass fails through avalanching of
 13 flanks producing a truncated cone-like deposit ('a' < 0.7) or conical deposit ('a' > 0.7). The

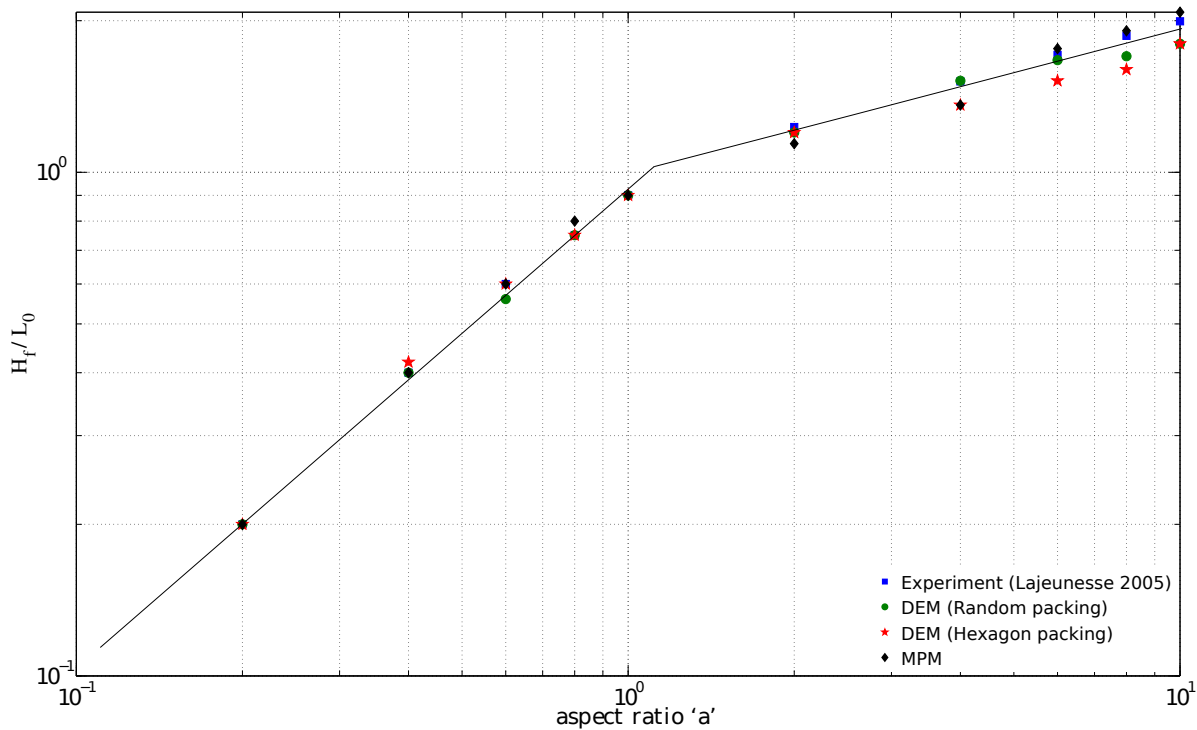


Figure 4.5 Normalised final collapse height for columns with different initial aspect ratio

grains located above the failure surface move “*en masse*” leaving a static region underneath the failure surface.

Dimensional analysis of granular column collapse reveals an intrinsic time defined as $\sqrt{H_i/g}$. This intrinsic time is a transient time of order τ_c , at which the flow is fully developed, i.e., the potential energy available at the initiation of collapse is now fully converted to kinetic energy. Numerical simulation of the velocity profile of a granular column ($'a'=0.4$) at critical time τ_c is presented in figure 4.6. At critical time, the velocity field depends only on the position of the grain along the sliding mass. The maximum velocity is observed at the front of the flowing mass corresponding to that of a plug flow in horizontal direction. Particulate and continuum simulations show similar run-out distance at the critical time. Both approaches show similar quantity of material destabilised above the failure surface. However, the crystalline arrangement of soil grains in a hexagonal packing results in a different flow mechanics, which also shows the effect of jamming at the flow front. The continuum nature of MPM results in a slightly different geometry of the material destabilised above the failure surface in comparison to DEM simulations. The velocity profile is similar to a steady granular surface flow observed by Lajeunesse et al. (2004).

For columns with lower initial aspect ratios, the run-out distance is proportional to the mass flowing above the failure surface. The spreading results from a Coulomb-like failure of the edges

and implies no free fall of the column. [Daerr and Douady \(1999\)](#) also observed active Coulomb yielding in transient granular surface flows. In this case, the effective friction properties of the flow can be simply predicted from the shape of the final deposit. The amount of mass mobilized during the collapse is significantly affected by the angle of the failure surface. Figure 4.6 shows that both numerical techniques predict a distinct failure surface when the flow is fully developed at critical time τ_c . The angle of the failure surface is found to be about 55° . The failure surface begins from the toe of the column and protrudes inwards at an angle of 50 to 55° . The formation of the “truncated conical deposit” or “conical deposit” depends only on the initial length of the column, as the angle of the failure surface is found to be independent of the aspect ratio. The failure angle is consistent with the interpretation in terms of *active Coulomb failure* ([Lajeunesse et al., 2004](#)), which leads to a predicted failure angle $\theta_y = 45^\circ + \delta/2$, where δ is the internal friction angle of the granular material. In the present study, the friction angle of the glass beads is 22° , which leads to $\theta_y = 45^\circ + 22^\circ/2 = 56^\circ$, which is in good agreement with the numerical simulations and experimental observations by [Lajeunesse et al. \(2004\)](#). The fracture angle has a direct effect on the transition between the truncated cone and the conical deposit occurring at an aspect ratio of 0.7. [Schaefer \(1990\)](#) observed the onset of instabilities in a narrow wedges of 56 to 65° for Cambridge-type constitutive models that describes granular flows, which is in-line with the failure angle observed in the present study.

The final profile of the granular column with an initial aspect ratio of 0.4 is shown in figure 4.7. Both MPM and DEM show similar run-out behaviour. The continuum approach is able to capture the flow dynamics of short columns, wher the failure mechanism is active Coulomb failure. In dense hexagonal packing, the failure surface is steep due to crystallisation effect. The variation in the angle of the failure surface causes a difference in the amount of material destabilised, and in turn in the run-out distance. This crystallisation phenomenon is found to have a significant influence on the final deposit of the granular column. [Lacaze and Kerswell \(2009\)](#) observed that poly-disperse grains have lesser tendency to crystallize especially in the case of tall columns.

For tall columns ($'a' > 2.3$), the flow is still initiated by a well defined failure surface as can be seen in figure 4.8. However, in this case the initial granular column is much higher than the top of the failure surface. Due to gravity most of the grains in the column experience free-fall consuming the column along their way. When they reach the vicinity of the failure surface, the flow gets deviated along the horizontal direction releasing a huge amount of kinetic energy gained during the free fall. For larger aspect ratio ($a > 0.7$), the resulting static region is a cone, the final height of the cone, i.e, H_f lies above the summit of the failure surface. Hence, a different evolution is observed from that of the axis-symmetric geometry ([Lube et al., 2005](#)), where the final height coincides with the summit of the failure surface forming a truncated

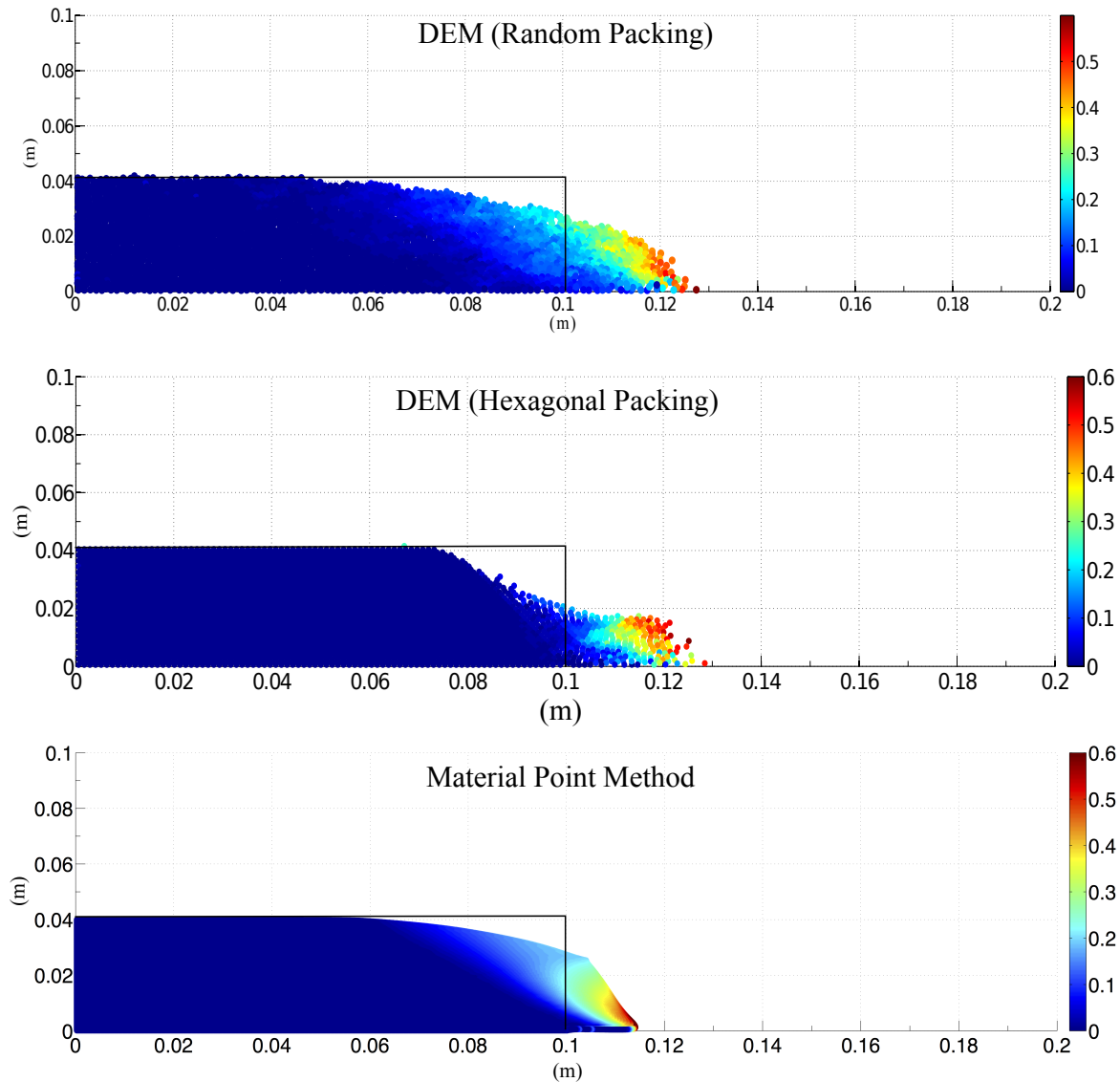


Figure 4.6 Velocity profile of a granular column collapse ($a' = 0.4$ & $t = \tau_c$)

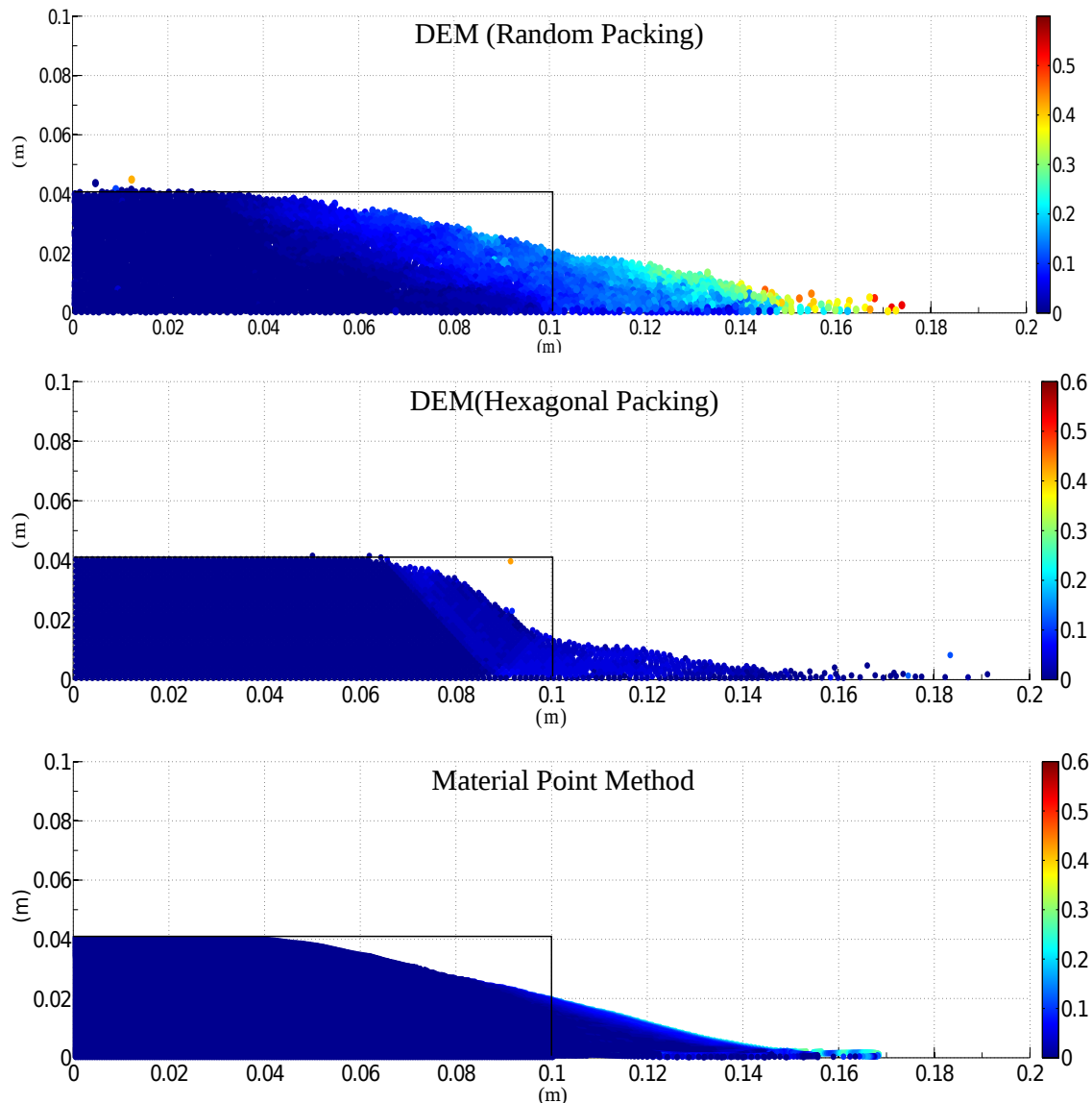


Figure 4.7 Velocity profile of a granular column collapse ($a' = 0.4$ & $t = 3 \times \tau_c$)

conical deposit. Lajeunesse et al. (2004) observed that the variation in the deposit morphology between the axis-symmetric case and the rectangular collapse to be a geometrical effect rather than as an experimental artefact.

An initial failure surface starting from the toe end of the column at an angle of about 55° can be observed at the critical time τ_c . As the collapse of the granular collapse progresses, successive failure planes parallel to the initial failure surface are formed and shear failure occurs along these planes. The presence of several shear bands in the final profile of the collapsed granular column confirms this hypothesis. Crystallisation in hexagonal packing has a significant effect on the run-out distance by forming series of parallel shear bands, resulting in unnatural flow kinematics. However, MPM exhibits a single failure surface. This observation throws light on the mechanics of propagation of shear bands in massive landslides such as the Storegga submarine landslide. The flow behaviour becomes similar to that of columns with lower aspect ratio as the flow starts descending along the failure plane. The final profile of the collapsed granular column with an initial aspect ratio of 6 is presented in Figure 4.9. For tall columns, the dissipation process is more complex due to the free-fall dynamics. The vertical acceleration of the grains induces a non-trivial mass distribution in the flow while spreading. This mass distribution plays a dominant role in the power-law scaling law obeyed by the run-out (Staron and Hinch, 2006).

Regardless of the experimental configuration and the initial aspect ratio of the columns, the flow is initiated by a well-defined rupture surface, above which the material slides down leaving a static region underneath the failure plane. Depending on the aspect ratio of the column, two asymptotic behaviours are observed. For smaller aspect ratios, the flow is dominated by friction where as large aspect ratio columns are influenced by the pressure gradient.

To study the influence of aspect ratio on the flow dynamics of granular columns, the flow front $L(t)$ and the maximum height of column $H(t)$ are tracked. The evolution of scaled height (H_f/L_0) and the run-out distance $(L_f - L_0)/L_0$ with time for granular columns with an initial aspect ratio of 0.4 and 6 are presented in figure 4.10. Three distinct regions can be observed in the flow evolution of a granular column collapse regardless of the initial aspect ratio of the column. An initial transient acceleration phase is observed for a time $0.8\tau_c$. This phase is followed by a heap movement of granular materials at the foot with a constant spreading velocity V for about $2\tau_c$. When time ‘ t ’ > τ_c , the velocity varies linearly with depth in the flowing layer and decreases exponentially with depth near the static layer. This velocity profile is similar to those observed in steady granular surface flows (Lajeunesse et al., 2004). Most of the run-out happens during this phase. The final phase involves deceleration of the flow front and the flow comes to rest after about $0.6\tau_c$. The spreading of the granular column ceases after a time in the order of about $3\tau_c$, however some motion still persists along the free surface

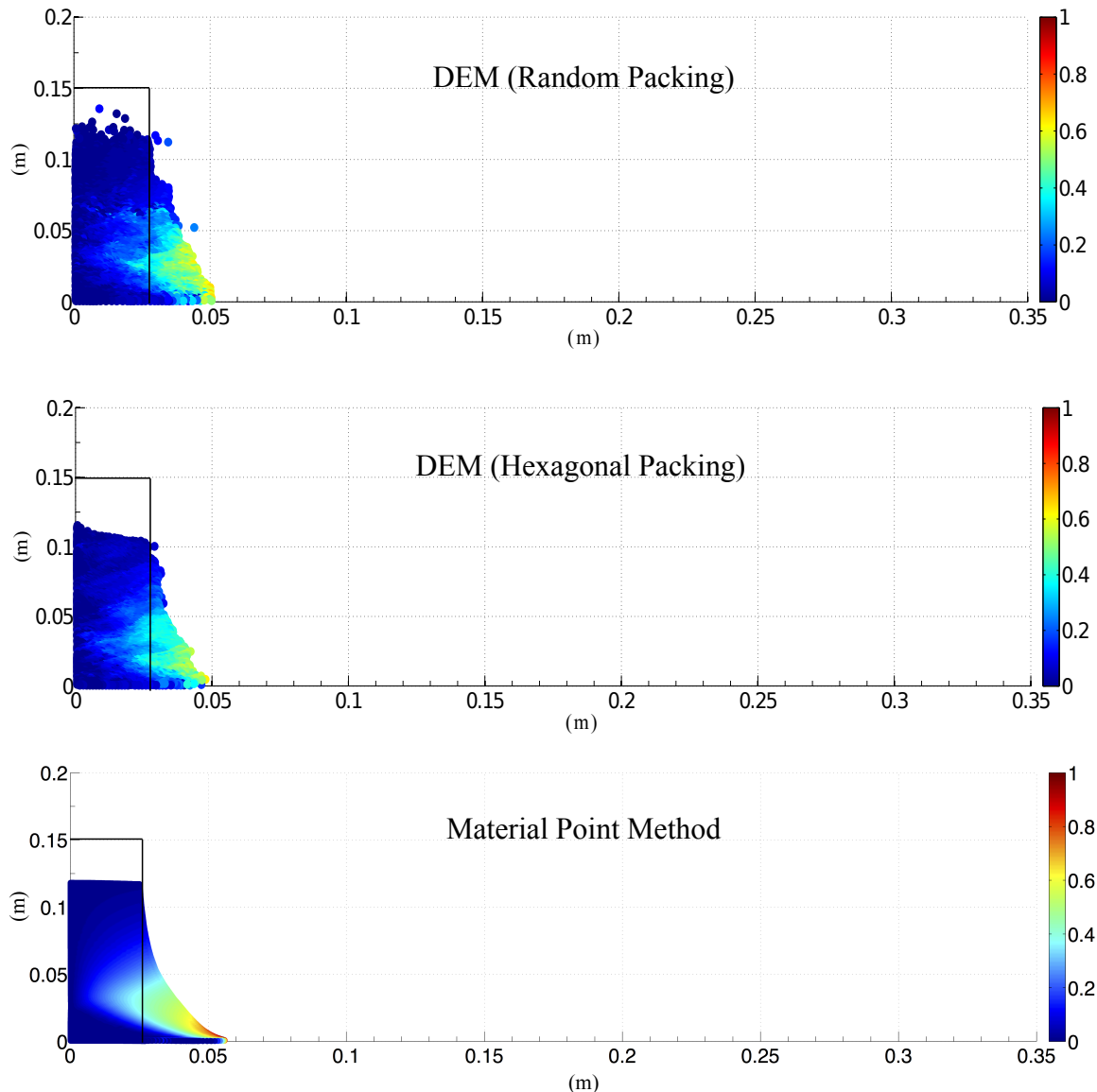


Figure 4.8 Velocity profile of a granular column collapse ($a' = 6$ & $t = \tau_c$)

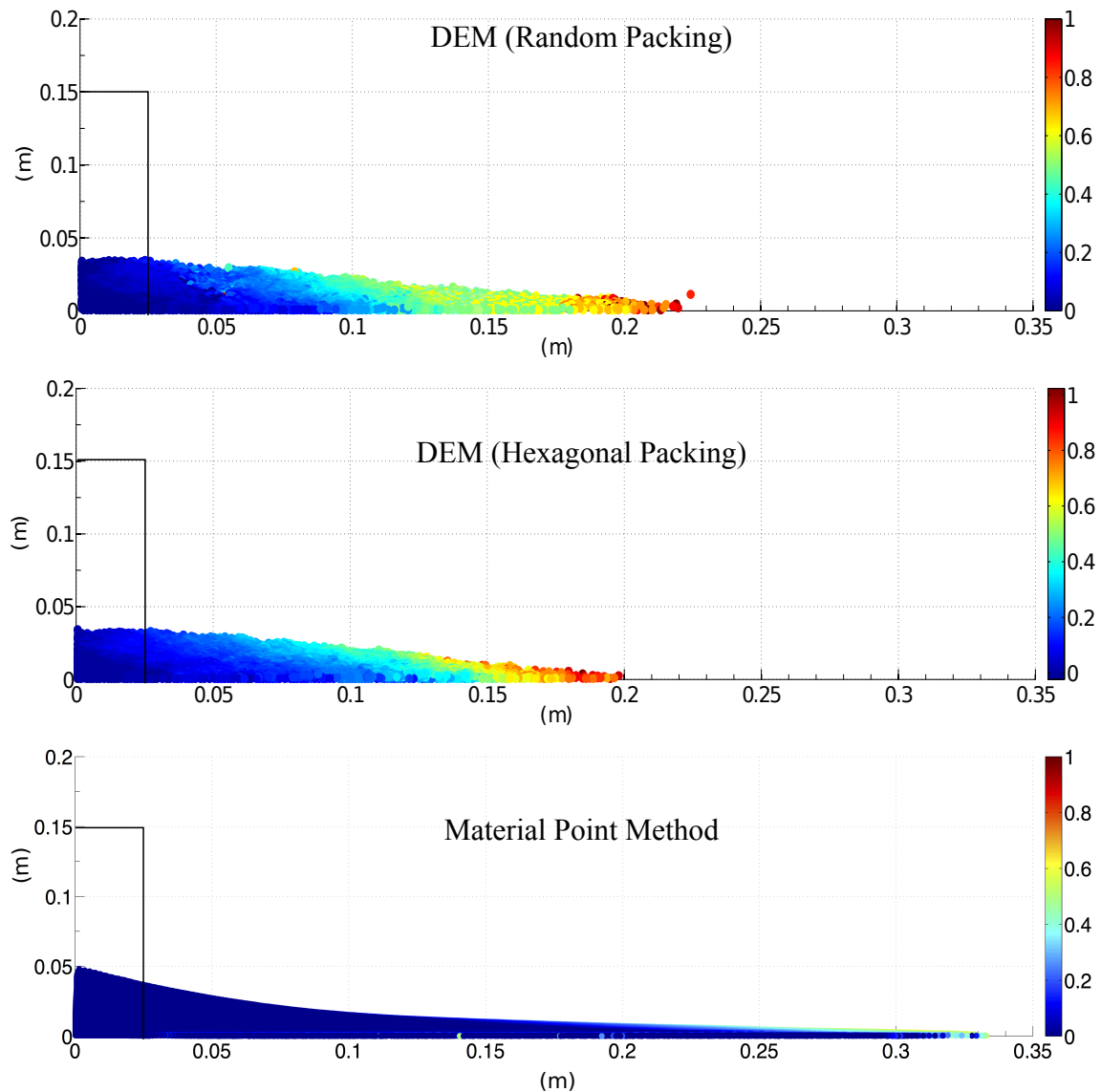


Figure 4.9 Velocity profile of a granular column collapse (' $a' = 6$ & $t = 3 \times \tau_c$)

1 behind the flow front for a much longer time due to internal rearrangement, the duration of
 2 which can last up to $t \approx 6\tau_c$.

3 The critical time is evaluated as the time at which the potential energy available for the flow
 4 has been converted to the kinetic energy. In short columns, the critical time observed in both
 5 hexagonal and random packing of grains matches the experimental observations. However, the
 6 Material Point Method overestimates the critical time by a factor of 1.25, which means that it
 7 takes longer for the flow to be fully mobilized. However, the actual run-out duration of the flow
 8 is short and the granular mass comes to rest at about $t = 3\tau_c$.

9 For columns with larger aspect ratios, the continuum and particulate approaches simulate
 10 similar flow evolution behaviour for times up to $3\tau_c$, beyond which particulate simulation
 11 decelerates and comes to rest, while the flow continues to evolve in MPM simulations resulting
 12 in longer run-out distance. The flow comes to rest at time $t = 6\tau_c$. The three phases in a
 13 granular flow can be distinctly observed in the flow evolution plot for a granular column with
 14 initial aspect ratio of 6 (see figure 4.10b). The flow evolution behaviour observed in the case of
 15 DEM simulation matches the experimental observation by Lajeunesse et al. (2004). Hexagonal
 16 packing predicts longer time for the flow to evolve, which can be attributed to crystallisation of
 17 grains. In MPM simulations, the failure starts at the toe of the column and slowly propagates up
 18 to form the failure surface. This results in slower initiation of the flow. It can be observed that
 19 MPM overestimates the critical time by 50%. Although, MPM and DEM simulations show the
 20 same run-out at time $t = 3\tau_c$, the flow evolution between both the approaches is different. MPM
 21 simulations continue to accelerate beyond $3\tau_c$ and ceases to flow at $6\tau_c$. In order to understand
 22 the difference in the flow dynamics in the case of Material Point Method it is important to study
 23 the mechanism of energy dissipation.

24 4.2.4 Energy dissipation mechanism

25 The energy dissipation mechanism during the collapse provides useful insight into the flow
 26 dynamics. In the case of small aspect ratios, the columns undergo no free fall. The spreading
 27 mainly results from the failure of the edges, while the top of the column remains essentially
 28 undisturbed in the central area. Staron and Hinch (2006) showed that the amount of energy
 29 dissipated during the spreading δE can be easily recovered using the simple shape of the final
 30 deposit and volume conservation (see figure 4.11). The difference of potential energy between
 31 the initial and the final states gives

$$32 \quad \delta E = \frac{1}{6} g \rho (L_f - L_0) H_0^2, \quad (4.8)$$

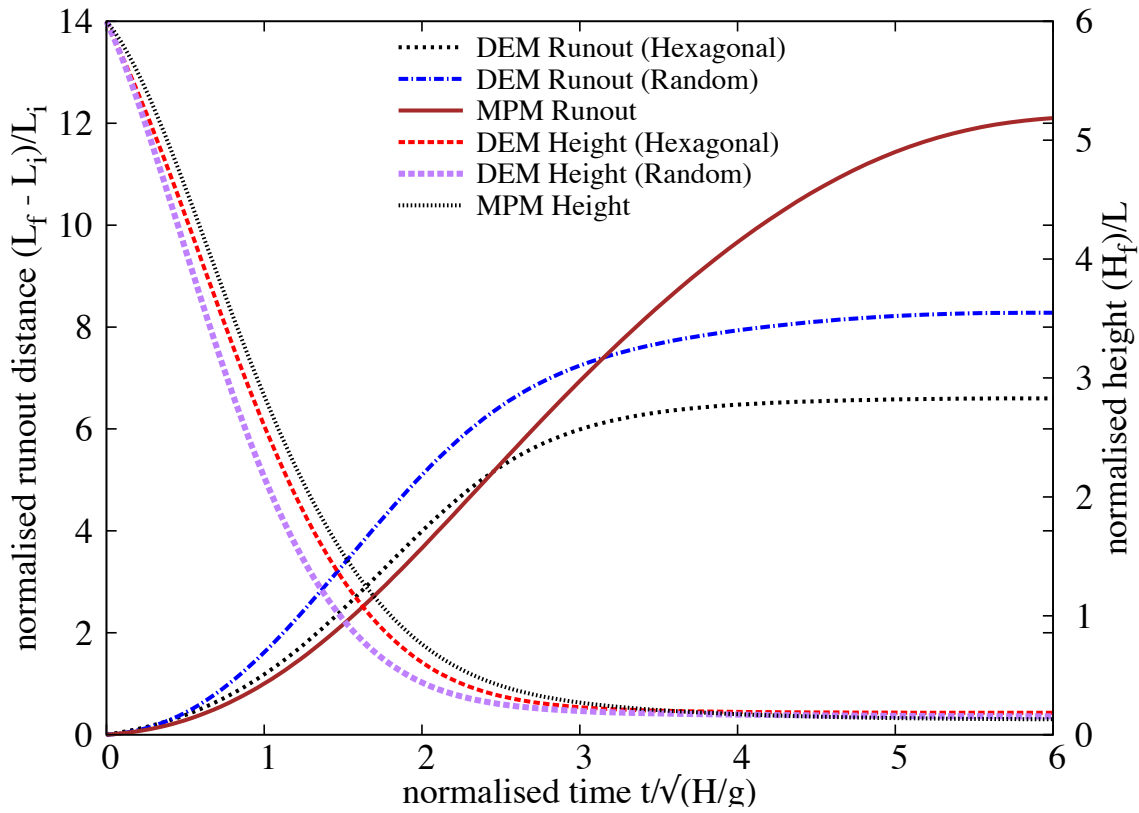
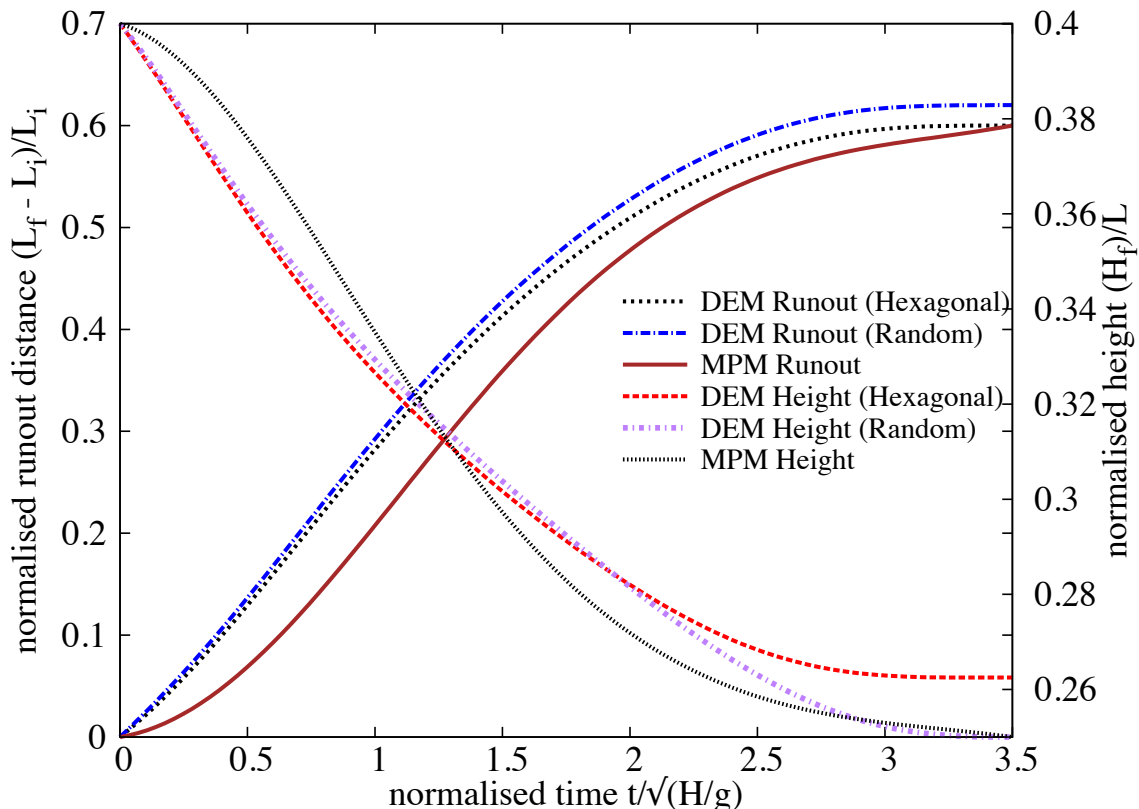


Figure 4.10 Flow evolution of granular column collapse

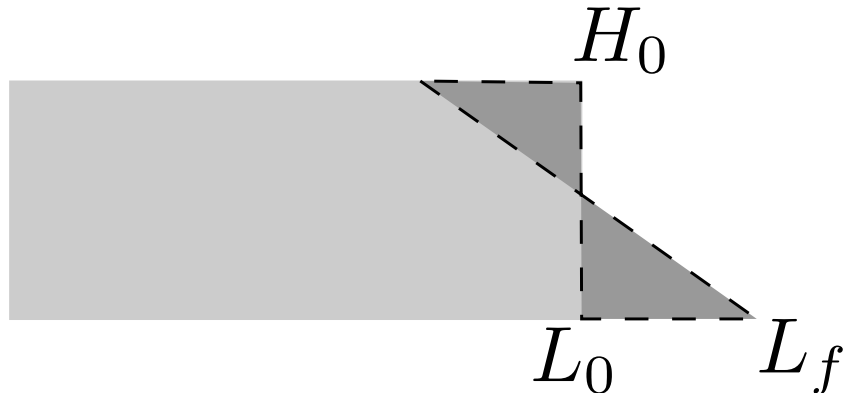


Figure 4.11 Scheme of collapse for small aspect ratio columns. The amount of energy δE lost in the process can be evaluated from the run-out distance $L_f - L_0$ (after [Staron and Hinch \(2006\)](#)).

where ρ is the density of the packing. It is assumed that this energy is dissipated by the work of friction forces W_μ over the total distance run by the center of mass G of the spreading material. [Staron et al. \(2006\)](#) considers two regions of dissipation: the amount of mass destabilised $\frac{1}{4}(L_f - L_0)H_0$ over two thirds of the runout distance $2(L_f - L_0)/3$ (considering the triangular shape of the final deposit and the initial and final positions of the center of mass). The effective coefficient of friction μ_e characterizes the mean dissipation in the flow. The work of friction forces is

$$W_\mu = \frac{1}{6}\mu_e g \rho (L_f - L_0)H_0^2, \quad (4.9)$$

Equating δE and W_μ gives $\mu_e(L_f - L_0) = H_0$. The scaling of the runout leads directly to the relation $\mu_e = \lambda^{-1}$, which is the numerical constant in the power law of the run-out that depends on the material properties ([Balmforth and Kerswell, 2005](#)). The amount of energy δE dissipated during the spreading is compared with $W = N_p g m_p r_p$, where N_p is the total number of grains, m_p is their mass, and r_p is the total horizontal distance run by each of them. We observe that the dissipation energy δE is proportional to W . [Staron and Hinch \(2006\)](#) observed that the coefficient of proportionality gives a measure of the effective friction and observed a power law dependence between μ_e and internal friction angle μ : $\mu_e = 0.425\mu^{0.2}$. The effective friction angle μ_e of 21° is observed, which is very close to the critical state friction angle of 22° used in MPM simulations. This proves that the energy dissipation mechanism modelled in a continuum sense as a frictional dissipation process captures the flow kinematics observed in DEM and experiments, for short columns.

[??](#) shows the time evolution of the normalised potential energy (E_p/E_0) and kinetic energy (E_k/E_0) for granular columns with initial aspect ratio ‘a’ = 0.4. The normalised potential and

kinetic energy are computed as

$$E_p = \sum_{p=1}^{N_p} m_p g h_p \quad (4.10) \quad 2$$

$$E_{ki} = \frac{1}{2} \sum_{p=1}^{N_p} m_p v_p^2 \quad (4.11) \quad 3$$

where N_p is the total number of particles, m_p is the mass of a particle ‘ p ’, h_p is the height and v_p is the velocity of the particle ‘ p ’. The cumulative dissipation energy is computed as

$$\frac{E_d}{E_0} = 1 - \frac{E_k}{E_0} - \frac{E_p}{E_0}. \quad (4.12) \quad 7$$

It can be observed that both MPM and DEM show similar energy dissipation mechanism. The DEM simulation shows 3% more potential energy dissipation in comparison with MPM simulations. This small difference in the potential energy is due to grain rearrangements. This shows the ability of continuum approach in capturing the flow kinematics of columns with small aspect ratios (‘ $a' \leq 2.3$ ’).

The evolution of normalised kinetic and potential energy of a tall column collapse (‘ a' of 6) is shown in figure 4.12b. It can be observed from the figure that the initial potential energy stored in the particle is converted to kinetic energy which is dissipated as the granular material flows down. Three successive stages can be identified in the granular column collapse. The flow is still initiated by a well defined failure surface. However, the centre of gravity of the granular column is much higher than the top of the failure surface, which results in free fall of grains under gravity consuming the column along their way. In this stage ($t < 0.8\tau_c$), the initial potential energy stored in the grains is converted into vertical motion. In the second stage, when the grains reach the vicinity of the failure surface, they undergo collisions with the bottom plane and the neighbouring grains, thus causing the flow to deviate along the horizontal direction releasing a large amount of kinetic energy gained during the free fall (see figure 4.9). In the third stage, the grains eventually leave the base area of the column and flow sideways (Lajeunesse et al., 2004). As the process involves collective dynamics of all the grains, it is difficult to predict the exact trajectory of a grain, however, the overall dynamics can be explained.

DEM simulations model both collisional and frictional dissipation process during the collapse of tall columns. However, MPM simulations assume that the total initial potential energy stored in the system is completely dissipated through friction over the entire run-out distance, this results in longer run-out distance. Figure 4.12b shows the evolution of energy with time. At the initial stage of collapse, characterised by free fall of grains under gravity,

1 DEM simulation due its particulate nature shows a rapid reduction in the potential energy in
 2 comparison with MPM, where the failure begins from the toe of the column. The continuum
 3 nature of MPM simulations results in slower initiation of collapse (see figure 4.10b). It can
 4 be also observed from figure 4.12b that dissipation energy in MPM is 25% less than DEM
 5 simulations. In order to understand the mechanism of energy dissipation, it is important to
 6 understand the contribution from the cumulative frictional and collisional parts. The frictional
 7 dissipation (basal and internal friction) observed in DEM is almost identical to the frictional
 8 dissipation observed in MPM. The difference in the dissipation energy is due to the collisional
 9 regime, which occurs at $0.8\tau_c$. The total and frictional dissipation curves diverge around $0.8\tau_c$
 10 where the grains near the vicinity of the failure surface undergo collisions with the bottom plane
 11 and the neighbouring grains resulting in collisional dissipation of the stored potential energy.
 12 DEM simulation show drop in the peak kinetic energy at $\approx 0.8\tau_c$, which is at the beginning
 13 collisional dissipate stage. MPM lacks this collision dissipation mechanism, which results in
 14 longer run-out distances for columns with large aspect ratios.

15 $\mu(I)$ rheology, discussed in ??, describes the granular behaviour using a dimensionless
 16 number, called the *inertial number I*, which is the ratio of inertia to pressure forces. Small
 17 values of I corresponds to critical state of soil mechanics and large values of I corresponds to
 18 the fully collisional regime of kinetic theory. $\mu(I)$ rheology is adopted in MPM simulations
 19 to understand the characteristics of the flow regime. Mohr-Coulomb model was used along
 20 with $\mu(I)$ rheology. Friction angle is changed according to the value obtained by Da Cruz
 21 et al. (2005) friction law that is dependent on the inertial number I as $\mu = \mu_{min} + bI$ where
 22 $\mu_{min} = 0.22$ and $b = 1$. Figure 4.13 shows the flow evolution of granular column collapse for
 23 aspect ratio ‘a’ of 0.4 and 6 using $\mu(I)$ rheology. For short columns, the evolution of flow based
 24 on $\mu(I)$ rheology is identical to the MPM simulation using Mohr-Coloumb model. However,
 25 for tall columns, $\mu(I)$ rheology evolves at the same rate as the DEM simulations up to $t = 0.8\tau_c$,
 26 after which MPM simulation continues to accelerate due to lack of collisional dissipation, while
 27 the DEM simulation decelerates with time.

28 Figure 4.15b shows that the short column attains a maximum inertial number of 0.012,
 29 which is in the dense granular flow regime, inertial number $I \approx 10^{-3}$ to 0.1 (Da Cruz et al.,
 30 2005). However, the maximum inertial number $I \approx 0.04$, for tall is still within the dense
 31 granular flow regime. DEM simulations, however, showed a collisional regime that has inertial
 32 number higher than 0.1. This shows that continuum approach using frictional laws are able to
 33 capture the flow kinematics at small aspect ratios, however are unable to precisely describe the
 34 flow behaviour for tall columns, which is characterised by an initial collisional regime.

4.2 Granular column collapse

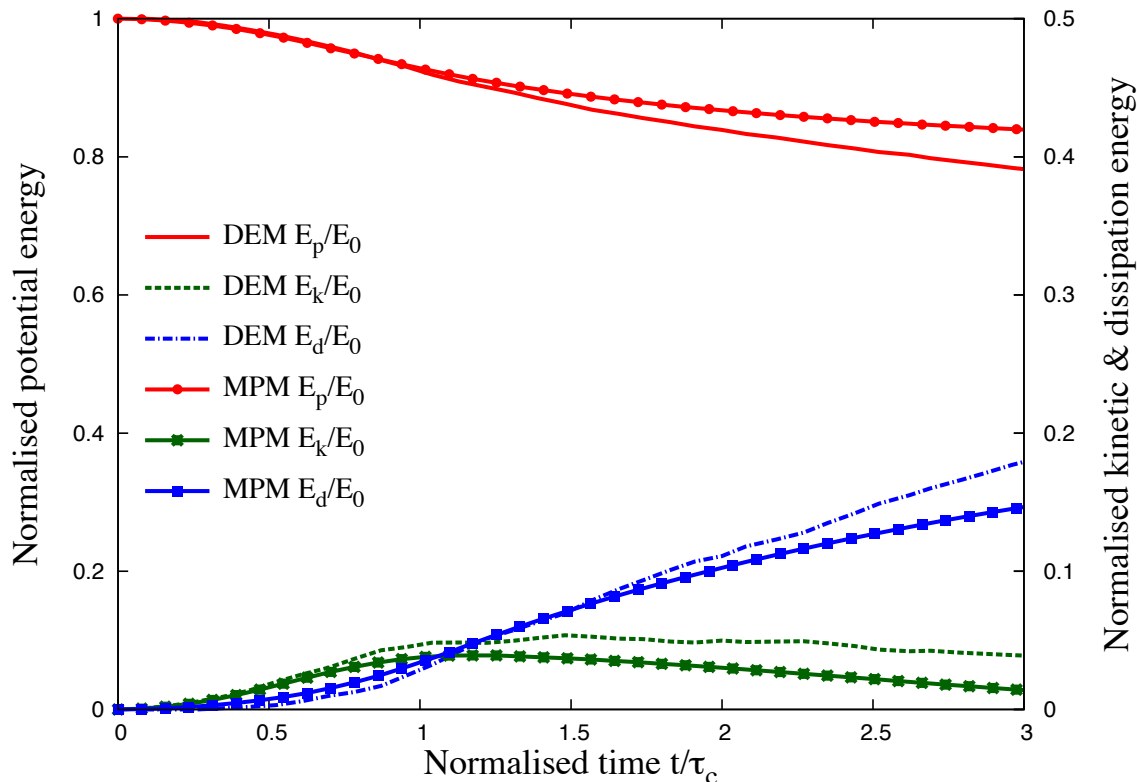
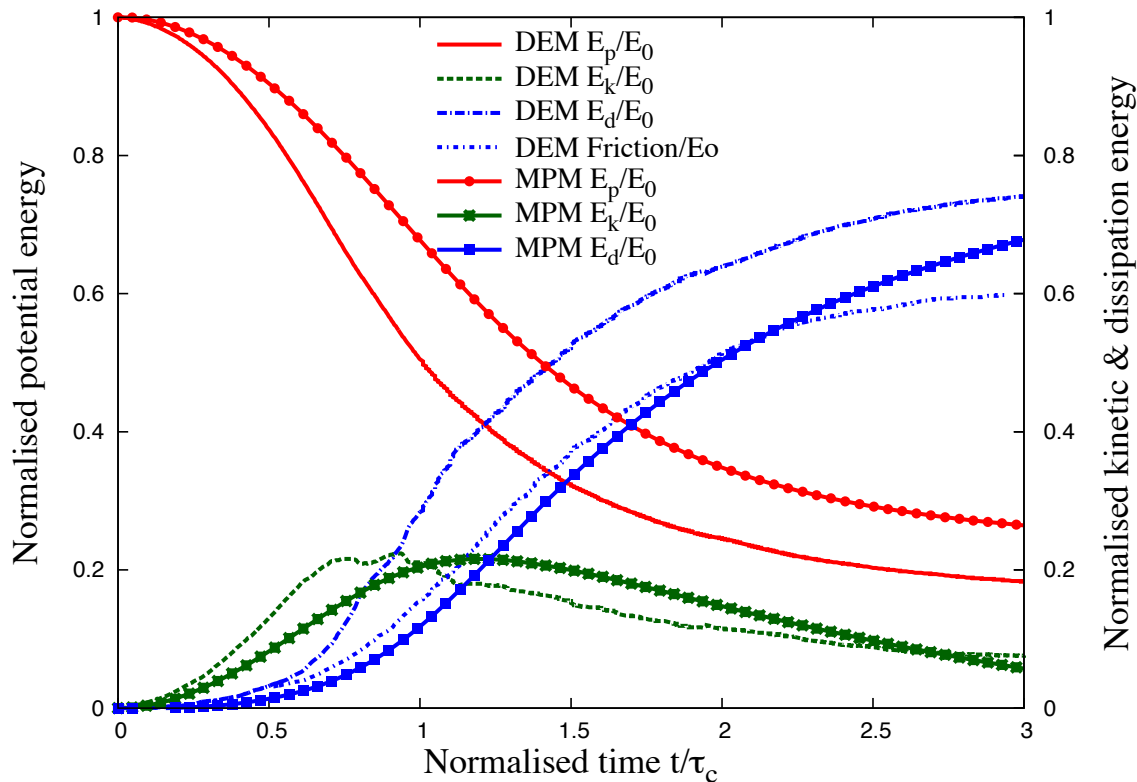
(a) Energy evolution of a column with ' a' = 0.4(b) Energy evolution of a column with ' a' = 6

Figure 4.12 Energy evolution of granular column collapse

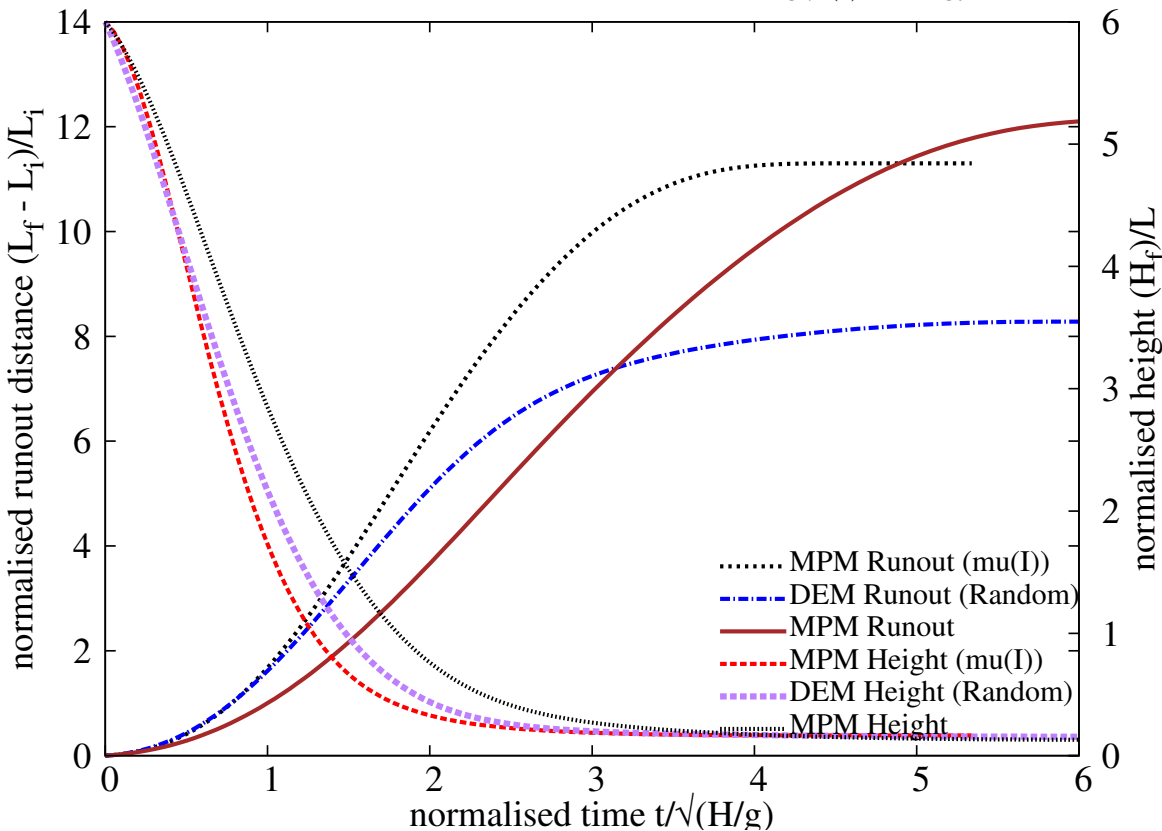
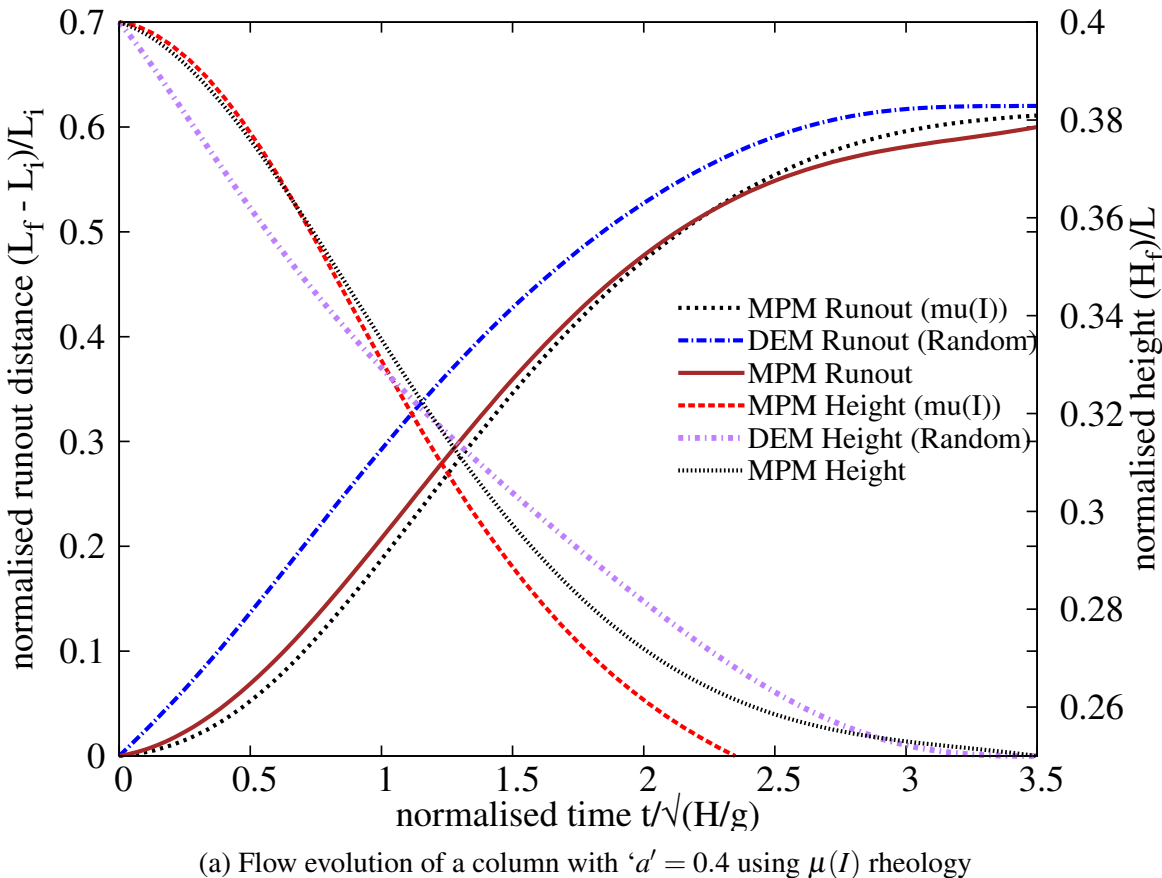


Figure 4.13 Flow evolution of granular column collapse using $\mu(I)$ rheology

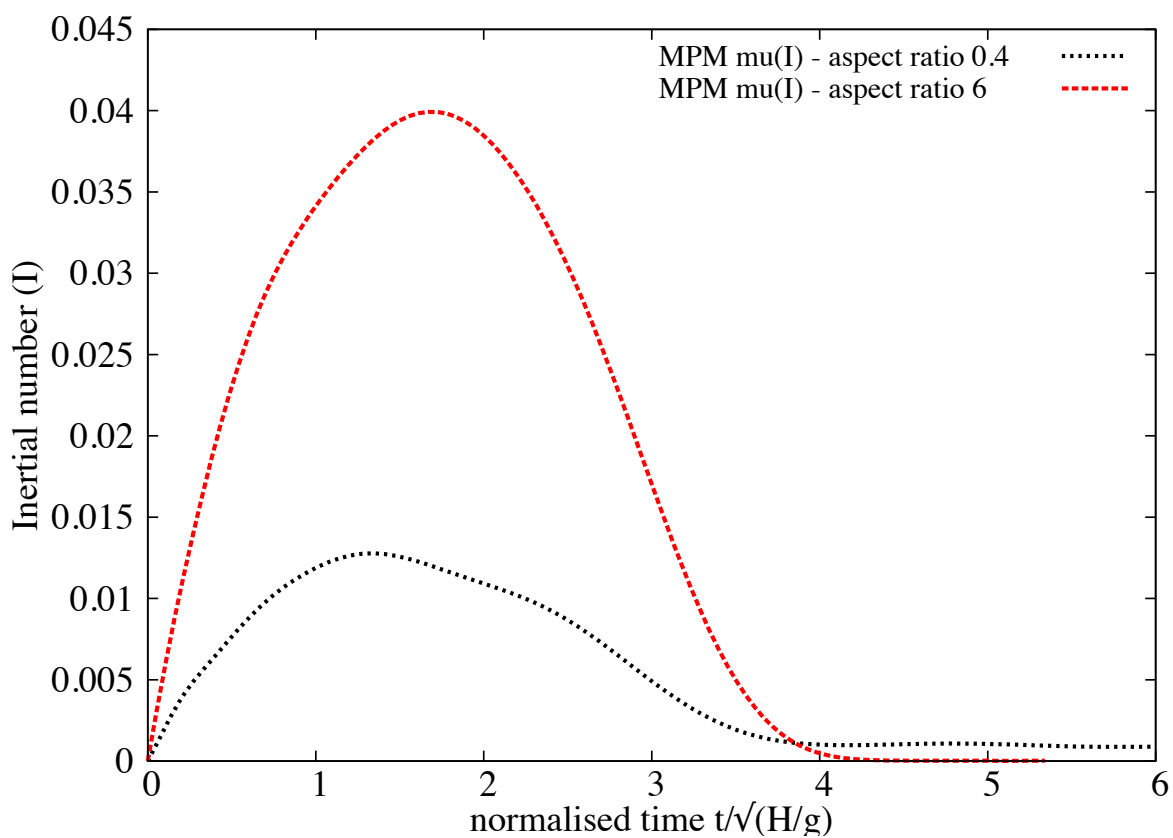


Figure 4.14 Evolution of inertial number with time for columns with ' $a' = 0.4$ and ' $a' = 6$

¹ 4.2.5 Numerical procedures

² The numerical samples are composed of ~ 13000 disks with a uniform distribution of diameters
³ by volume fractions in the range $[d_{min}, d_{max}]$ with $d_{max} = 1.5d_{min}$. The mean particle diameter
⁴ and mass are $d \simeq 0.0025$ m and $m \simeq 0.0123$ kg, respectively. The particles are first poured
⁵ uniformly into a rectangular box of given width and then the right-hand side wall is shifted
⁶ further to the right to allow the particles to spread. A half-pile is obtained when all particles
⁷ come to rest; see ^{??}. This procedure leads to a mean packing fraction $\simeq 0.83$.

Table 4.4 DEM simulation of simple shear test ([?])

Parameter	Value
Mean grain diameter	≈ 2.455 mm
Grain diameter $[d_{min} : d_{max}]$	[2.0, 3.0] mm
Friction coefficient	0.4
Grain density	2600kg m^{-3}
Restitution coefficient	0
Number of grains	1174

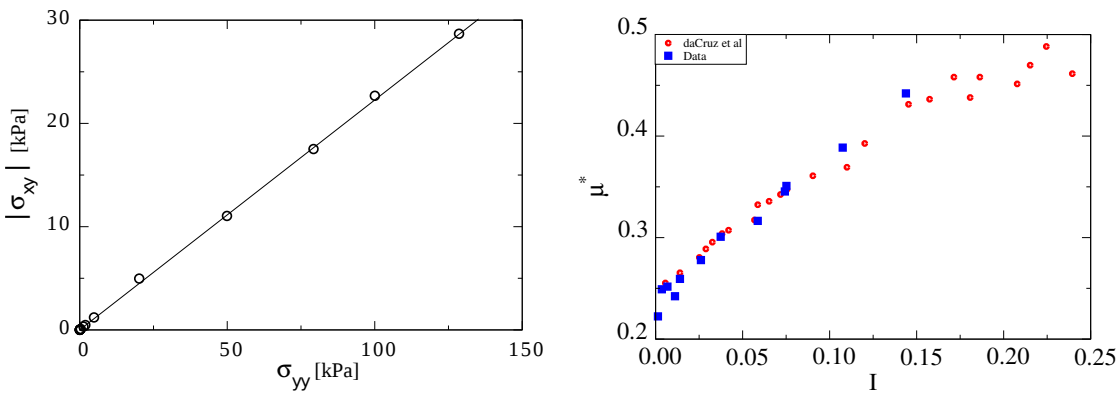
⁸ The initial static pile is set into motion by applying a constant horizontal gradient $v_{0x}(y) =$
⁹ $k(y_{max} - y)$ with $k > 0$. Such a configuration mimics the energy transfer mechanism of a
¹⁰ horizontal quake along the bottom of the pile. We are interested in the evolution of the
¹¹ geometry of the pile and its total kinetic energy as a function of the initial input energy E_0 . The
¹² run-out distance R_f is the distance of the rightmost particles from the left wall when the pile
¹³ comes to rest. It will be normalized by the initial extension R_0 of the pile, as in the experiments
¹⁴ of collapsing columns. The total run-out duration t_f is the time that the pile takes to reach its
¹⁵ final run-out distance R_f .

¹⁶ The initial static pile is set into motion by applying a horizontal velocity $v_{0x}(y)$ to all
¹⁷ particles during a short interval of time. Different velocity fields were tested: 1) The same
¹⁸ velocity $v_{0x}(y) = v_0$ applied to all particles, 2) The same velocity $v_{0x}(y) = v_0$ applied to a
¹⁹ column of particles next to the left wall, 3) a constant velocity gradient $v_{0x}(y) = k(y_{max} - y)$
²⁰ with $k > 0$. The first two pushing modes mimic the case of a pile impacted from the left
²¹ by a moving mass (tsunami, debris...) whereas the last mode represents energy transfer by
²² horizontal quake of the bottom line. We will compare briefly below the effect of different
²³ pushing modes, but later we will mainly explore the third mode. We are interested in the
²⁴ evolution of the geometry of the pile and its total kinetic energy as a function of the initial
²⁵ energy input E_0 . The run-out distance R_f is the distance of the rightmost particles from the left
²⁶ wall when the pile comes to rest. It will be normalized by the initial extension R_0 of the pile, as

in the experiments of collapsing columns. The total run-out duration t_f is the time that the pile takes to reach its final run-out distance R_f .

For grain scale simulations, classical DEM and Contact Dynamics approach is used. A detailed description of the Contact Dynamics method can be found in [Jean \(1999\)](#); [Radjai and Dubois \(2011\)](#); [Radjai and Richefeu \(2009\)](#); [?](#). This method is based on implicit time integration of the equations of motion and a nonsmooth formulation of mutual exclusion and dry friction between particles. The CD method requires no elastic repulsive potential and no smoothing of the Coulomb friction law for the determination of forces. For this reason, the simulations can be performed with large time steps compared to discrete element simulations. The unknown variables are particle velocities and contact forces, which are calculated at each time step by taking into account the conservation of momenta and the constraints due to mutual exclusion between particles and the Coulomb friction. We use an iterative research algorithm based on a nonlinear Gauss-Seidel scheme. The only contact parameters within the CD method are the friction coefficient μ_s , the normal restitution coefficient e_n and the tangential restitution coefficient e_t between particles. We will investigate the effect of these parameters on the evolution of kinetic energy and the profile of the pile.

The natural units of our system are the mean particle diameter d , mean particle mass m and gravity g . For this reason, in the following we normalize the lengths by d , the times by $(d/g)^{1/2}$, the velocities by $(gd)^{1/2}$ and the energies by mgd .



(a) Evaluating the critical state friction angle from periodic shear test. (b) Evolution of Inertial number with friction μ

Figure 4.15 Periodic shear test using CD ([?](#)).

4.2.6 Evolution of pile geometry and run-out

In this section, we consider the spreading process following the initial energy input into the pile. Fig. ?? shows several snapshots of the pile for an initial input energy $E_0 = 61$ (in dimensionless

1 units). The pile is sheared from the bottom to the top, thus leaving a cavity in the vicinity of
2 the left wall. The cavity is partially filled while the pile continues to spread to the right.

3 In this section, we consider the spreading process following the initial energy input into the
4 pile. Fig. ?? shows several snapshots of the pile for each pushing mode and for the same initial
5 energy $E_0 = 61$ (in dimensionless units). In mode 1, where the same velocity is imparted to all
6 particles, the whole pile moves away from the left wall over a short distance and then it spreads
7 out and declines in slope. The spreading continues farther until the slope nearly declines to
8 zero. In mode 2, where the velocity is applied to a column of particles next to the left wall, the
9 particles belonging to the column are literally expelled from the pile. They fall back farther
10 way on the pile after a ballistic travel above the pile. At the same time, the right side of the pile
11 slightly spreads away while the left side is filled by the particles rolling down into the gap left
12 by the column. In mode 3, the pile is sheared from the bottom to the top, leaving thus a cavity
13 in the vicinity of the left wall. The cavity is partially filled while the pile continues to spread.

14 All pushing modes involve a transient with a sharp change of the geometry of the pile
15 followed by continuous spreading to the right. In mode 2, most of the energy is carried away by
16 the ejected particles. In mode 1, the pile has a rigid-body velocity component and moves away
17 from the left wall, but shows an efficient energy transfer leading to a long run-out distance. The
18 transient is more energy consuming in mode 3 compared to mode 1. For this reason, the run-out
19 distance in mode 3 is long but shorter than in mode 1. In the following, we analyze in more
20 detail the evolution of the pile in mode 3, which mimics a horizontal quake from the bottom
21 and, despite the creation of a cavity, remains always in contact with the left wall irrespective of
22 the input energy.

23 Figure 4.4 shows the normalized run-out distance $(R_f - R_0)/R_0$ and total run-out time t_f as
24 a function of the input energy E_0 . We observe two regimes both characterized by a power-law
25 run-out distance and time as a function of E_0 . In the first regime, corresponding to the range of
26 low input energies $E_0 < 40 \text{ mgd}$, the run-out distance varies as $R_f \propto (E_0)^\alpha$ with $\alpha \simeq 0.61 \pm 0.04$
27 over nearly one decade while the duration keeps a constant value $t_f \simeq 60 (d/g)^{0.5}$ irrespective
28 of the value of E_0 ! The error on the value of the exponent represents the confidence interval
29 of linear fits on the logarithmic scale. An average run-out speed can be defined from the ratio
30 $v_s = (R_f - R_0)/t_f$. According to the data, we have $v_s \propto (E_0)^{0.61 \pm 0.04}$. Since the initial average
31 velocity varies as $v_0 \propto (E_0)^{0.5}$, this difference between the values of the exponents suggests
32 that the mobilized mass during run-out declines when the input energy is increased. As we
33 shall see below, the constant run-out time reflects also the collapse of the particles into the
34 cavity left behind the pile.

35 In the second regime, corresponding to the range of high input energies $E_0 > 40 \text{ mgd}$,
36 the run-out distance varies as $R_f \propto (E_0)^{\alpha'}$ over one decade with $\alpha' \simeq 0.77 \pm 0.03$ while the

duration increases as $t_f \propto (E_0)^{\beta'}$ with $\beta' \simeq 0.21 \pm 0.04$. Hence, in this regime the average run-out speed varies as $v_s \propto (E_0)^{0.56 \pm 0.07}$. This exponent is close to the value 0.5 in $v_0 \propto (E_0)^{0.5}$, and hence, within the confidence interval of the exponents, in the second regime we may assume $\beta' \simeq \alpha' - 0.5$ and $v_s \propto v_0$.

It is worth noting that a similar power-law dependence of the run-out distance and time were found in the case of collapsing columns of grains with respect to the initial aspect ratio Topin et al. (2012). In the column geometry, the particles spread away owing to the kinetic energy acquired during gravitational collapse of the column. Topin et al. found that the run-out distance varies as a power law of the available peak kinetic energy at the end of the free-fall stage with an exponent $\simeq 0.5$. This value is below those obtained here for both regimes. This is, however, physically plausible since the distribution of particle kinetic energies at the end of the collapse is more chaotic than in our simulations where the energy is supplied from the very beginning in a well-defined shear mode. As pointed out by Staron et al. (2005), the distribution of kinetic energies is an essential factor for the run-out distance.

4.2.7 Decay of kinetic energy

The non-trivial evolution of the pile geometry in two regimes suggests that the energy supplied to the pile is not simply dissipated by shear and friction with the bottom plane. We also need to split the kinetic energy into its different components (x , y and rotation) of the velocity field. The input energy is in the x component, but due to both the creation of a cavity next to the left wall and the rolling of the particles down the free surface of the pile and between particles, a fraction of the energy is first transferred to the y component of the velocity field and dissipated during the transient. In this section, we analyse these features in order to arrive in a picture consistent with the evolution of the pile shape.

The decay of the total kinetic energy E is displayed in ??(a) for values of the input energy E_0 . We observe an initial fast drop of E followed by a regular fall-off until the end of the run-out. This regular fall-off occurs clearly with two different functional forms, thus revealing two stages in the evolution of the pile. ??(b) shows the same plots normalized by E_0 . We see that all plots corresponding to the first regime (low energies) collapse nearly on to a single time evolution. This is consistent with the fact that, as previously shown, in this regime the run-out time t_f is independent of the input energy. In contrast, the plots corresponding to the second regime (high energies) collapse only at the beginning of run-out, i.e. for $t < t_1 \simeq 7.5 (d/g)^{0.5}$.

?? displays the evolution of kinetic energy in the translational (E_x and E_y) and rotational (E_θ) degrees of freedom of the particles. E_x decays as the total energy, but E_y and E_θ increase and pass through a peak before decaying rapidly to a negligibly small level. The transient is best observed for E_y , which has significant values only for $t < t_1$. This energy represents the

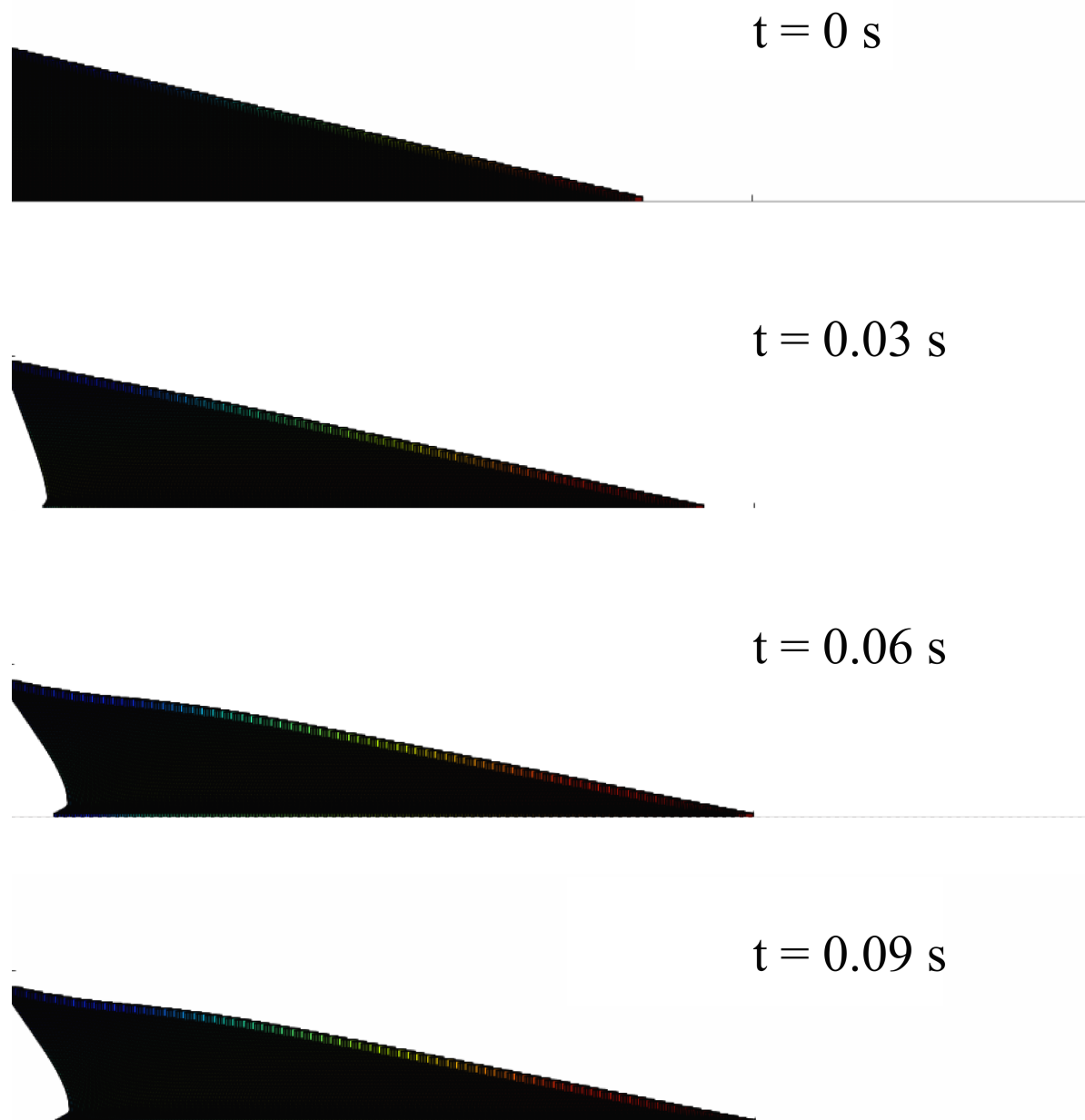


Figure 4.16 Snapshots of MPM simulations of the evolution of granular pile subjected to a gradient impact energy.

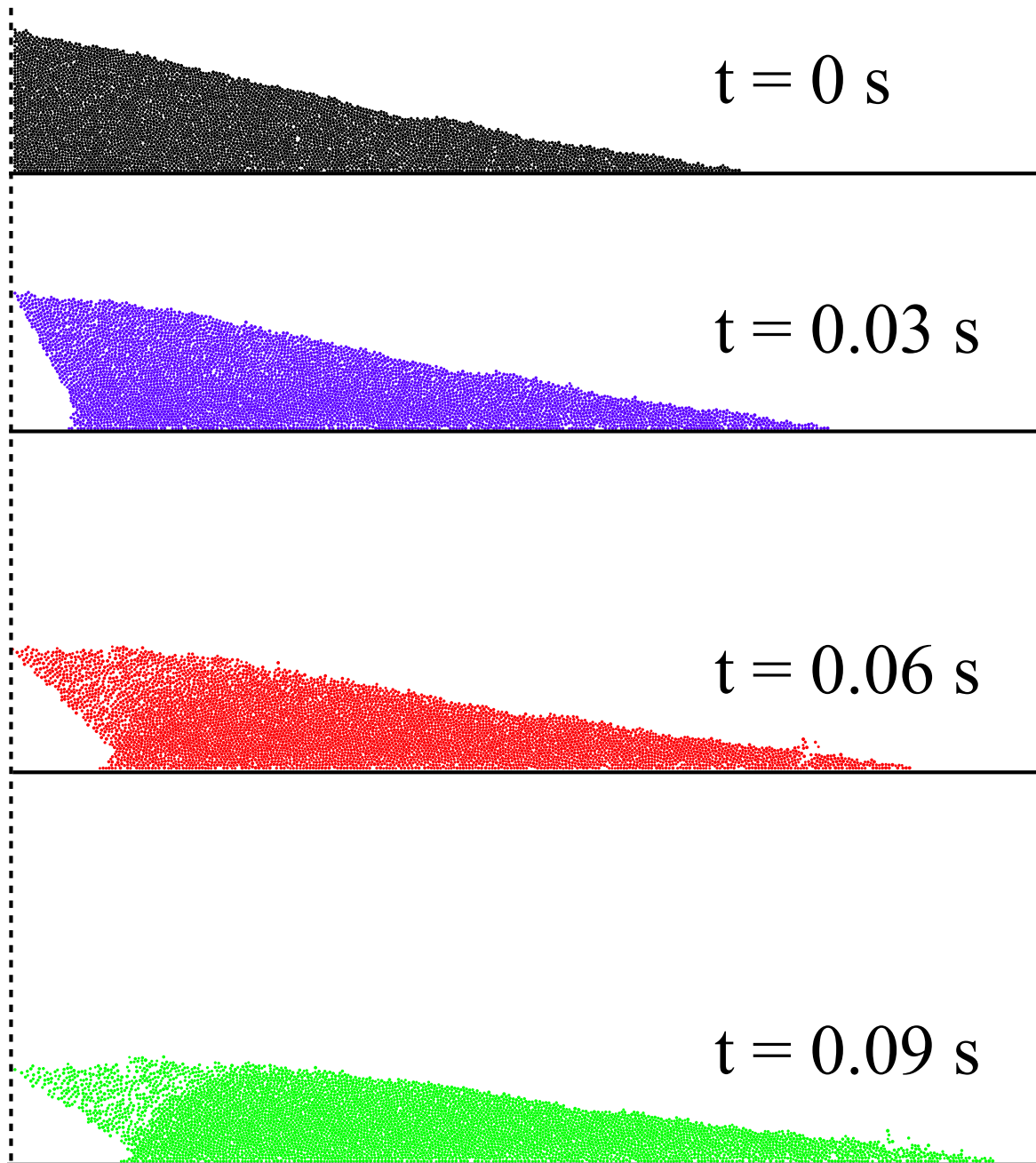


Figure 4.17 Snapshots of CD simulations of the evolution of granular pile subjected to a gradient impact energy (?).

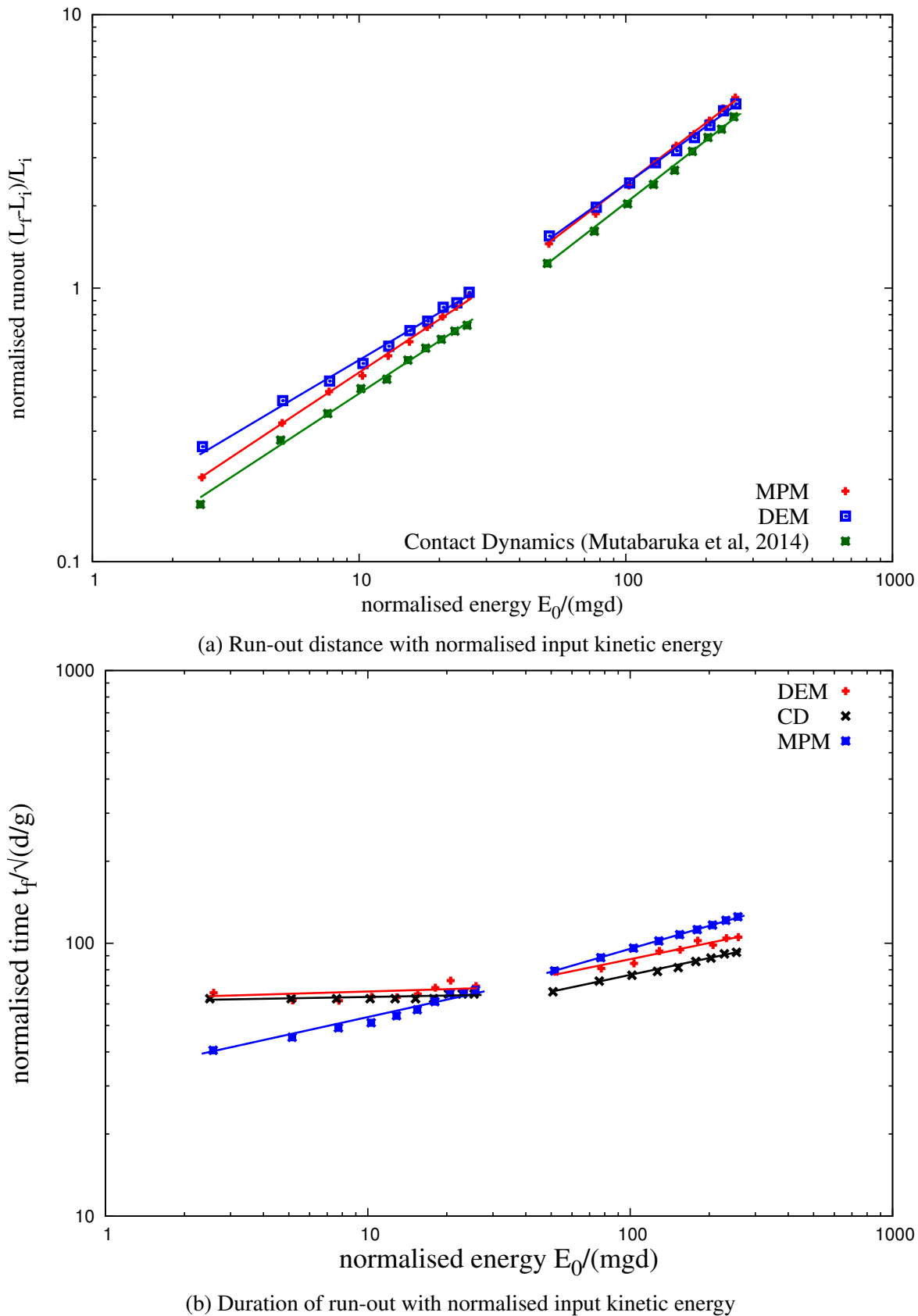


Figure 4.18 Run-out behaviour of a pile subjected a gradient impact energy

4.2 Granular column collapse

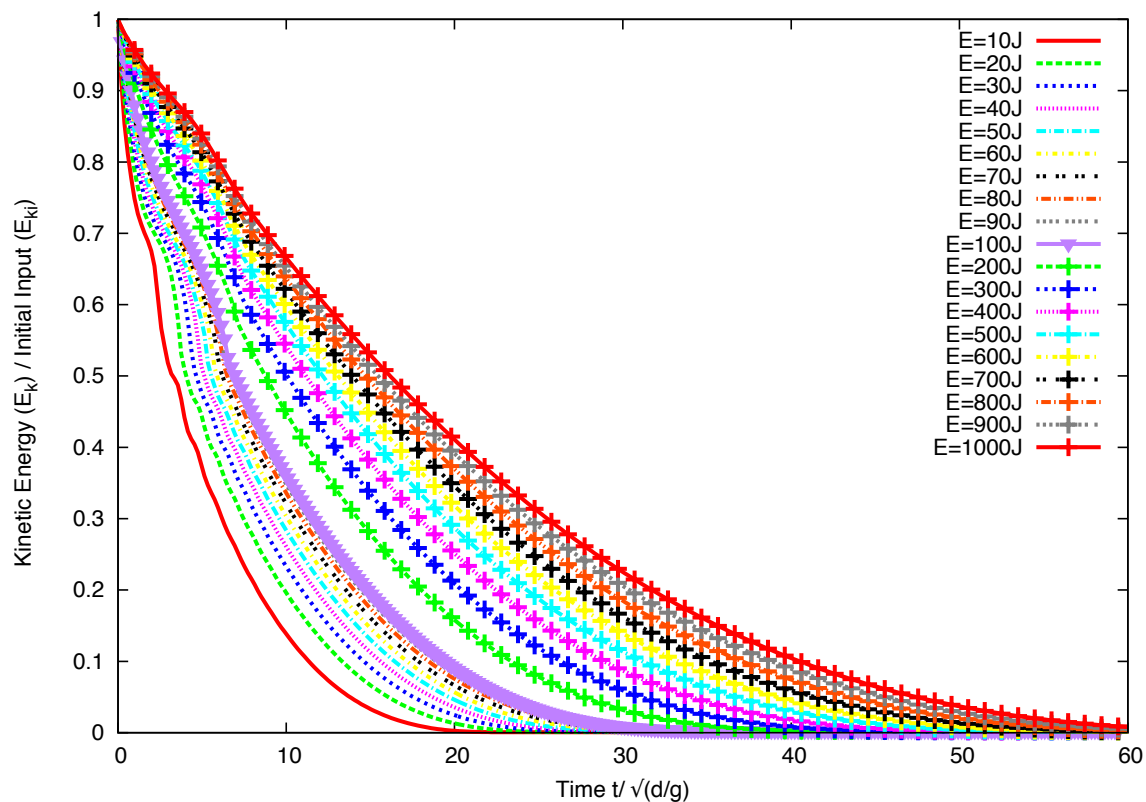
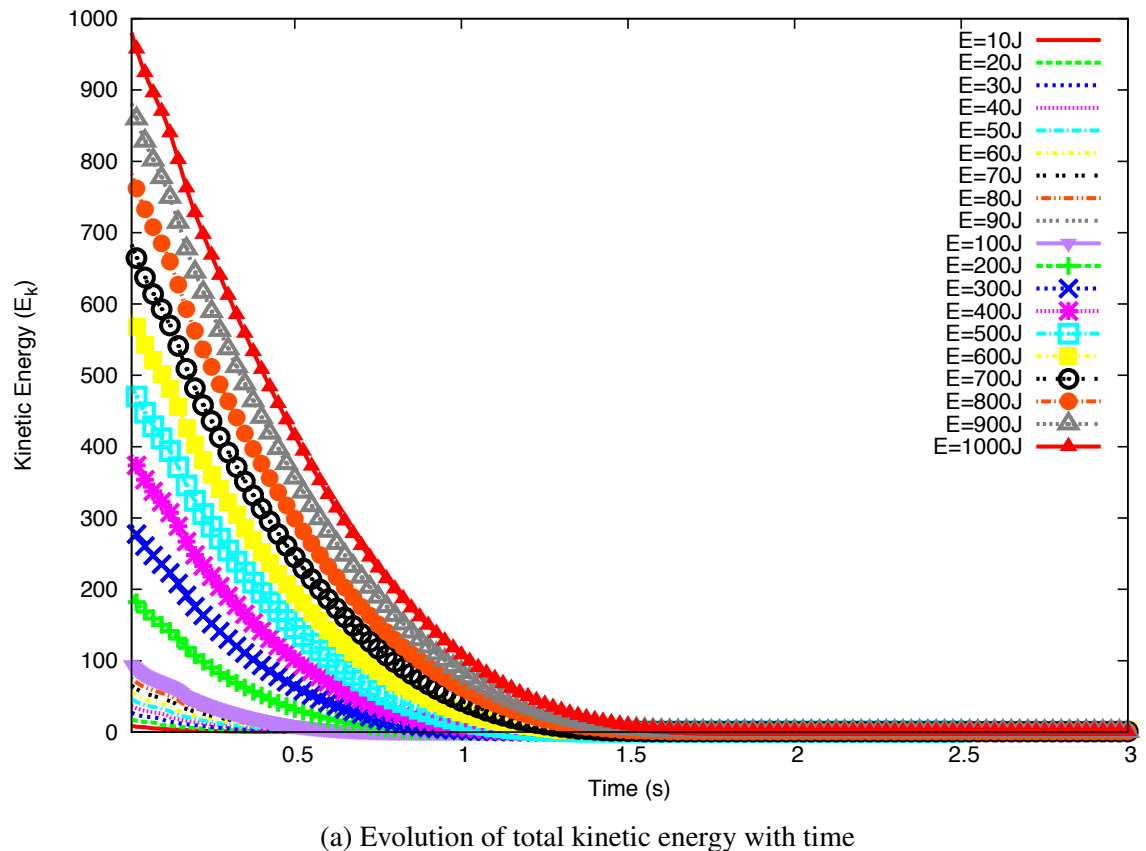


Figure 4.19 Evolution of kinetic energy with time

proportion of kinetic energy transferred to the y component of the velocity field due to the destabilization of the pile and collapse of particles in the cavity behind the pile. We note that the lower E_0 , the higher the peak value of E_y/E_0 . This means that, at low values of the input energy a larger fraction of input energy E_0 is consumed in the destabilization process whereas at a high level of input energy, most of it is dissipated in the spreading phase. For this reason, the total duration t_1 of this destabilization transient is nearly the same in both regimes and its value is controlled by the gravity rather than the input energy. The height of the pile being of the order of $80 d$, the total free-fall time for a particle located at this height is $\simeq 12 (d/g)^{0.5}$, which is of the same order as t_1 . As to the rotational energy, its contribution both to the transient stage and spreading appears to be negligible.

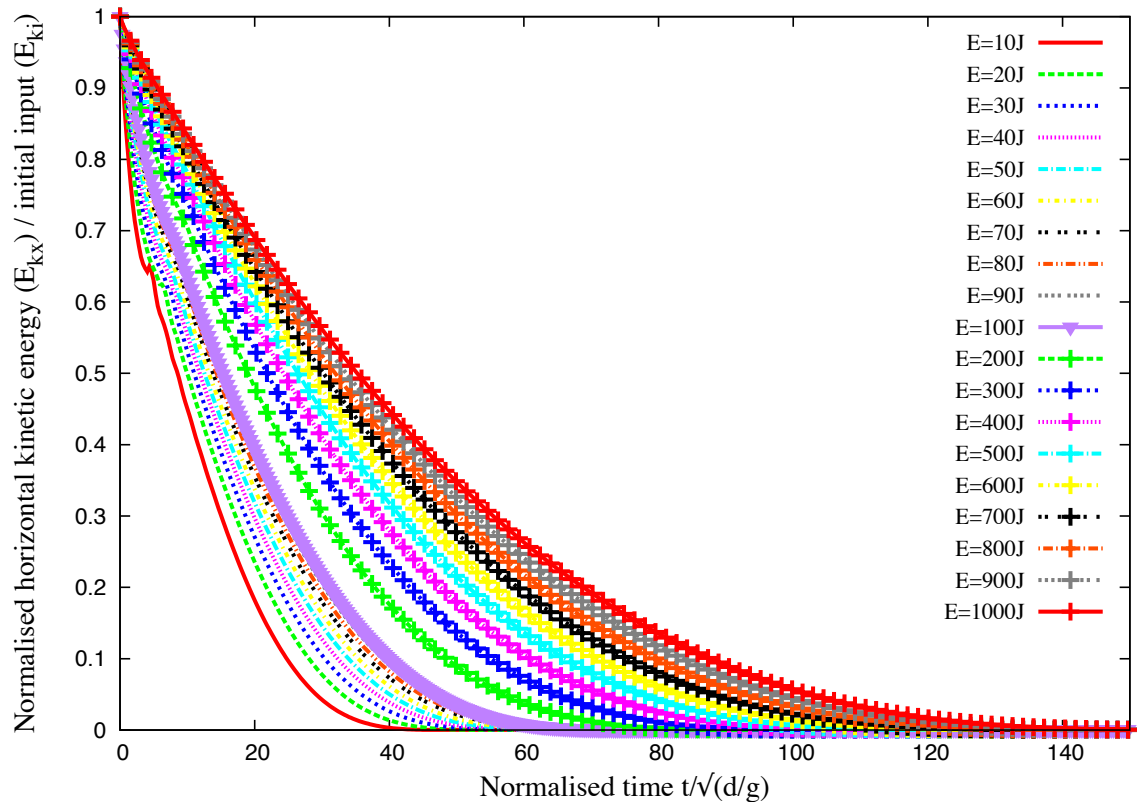
To analyze the second phase in the second regime, we now consider only the kinetic energy E'_{x0} available at the end of the transient. This energy is responsible for most of the run-out and hence it is expected to control the run-out distance and time. Fig. ??(a) shows the evolution of E_x normalized by E'_{x0} as a function of time. The plots have seemingly the same aspect but they show different decay times. A decay time τ can be defined as the time required for E_x to decline by a factor $1/2$. Fig. ??(b) shows the same data in which the time t' elapsed since t_1 is normalized by τ . Interestingly, now all the data nicely collapse on the same curve. We checked that this curve can not be fitted by simple functional forms such as variants of exponential decay. This means that the spreading of the pile is not a self-similar process in agreement with the fact that the energy fades away in a finite time t'_f .

The scaling of the data with the decay time τ suggests also that the run-out time t'_f since the beginning of the second phase might be a simple function of τ . Figure 4.21 shows both t'_f and τ as a function of E'_{x0} , where we observe a power law for both times over nearly one decade. The run-out time $t'_f \propto (E'_{x0})^{\beta'}$ has the same exponent $\beta' \simeq 0.21 \pm 0.03$ as t_f as a function of E_0 (see Fig. 4.4). For the decay time we have $\tau \propto (E'_{x0})^{\beta''}$ with $\beta'' \simeq 0.28 \pm 0.03$. The relation between the two times can thus be expressed as

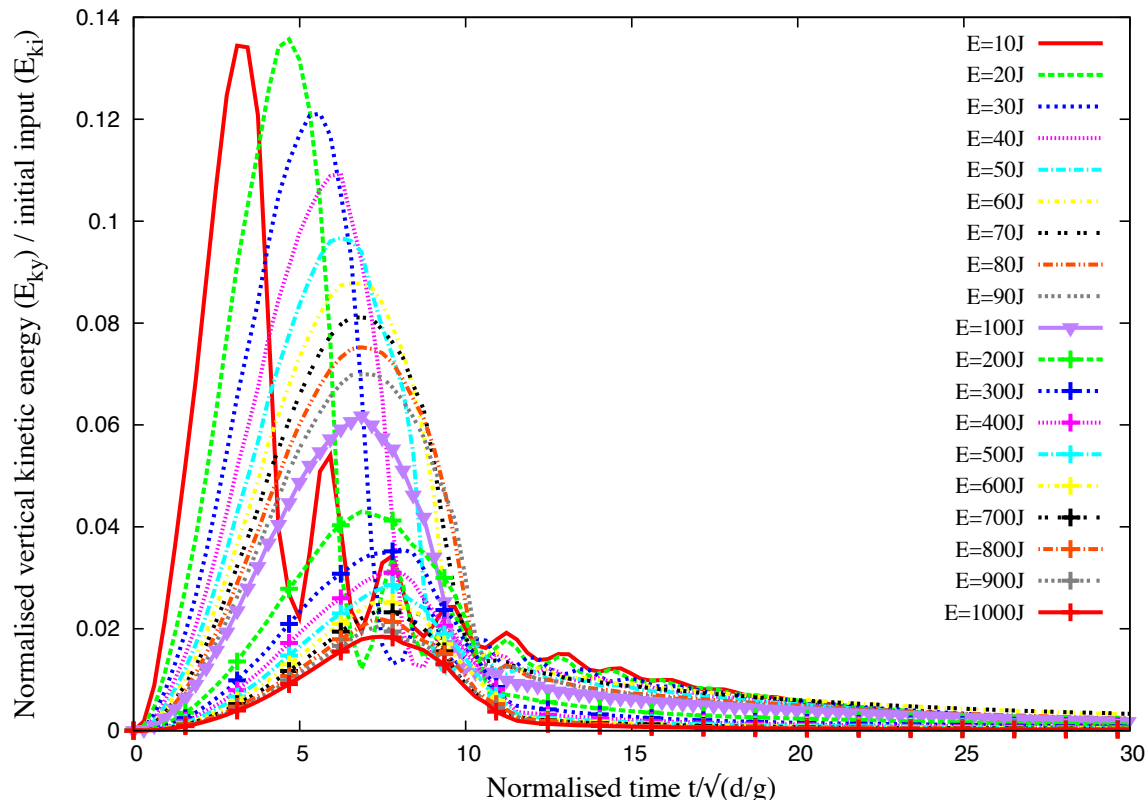
$$t'_f = k \tau (E'_{x0})^{\beta'' - \beta'}, \quad (4.13)$$

where $k \simeq 5 \pm 0.4$ and $\beta'' - \beta' \simeq -0.05 \pm 0.06$. This value is small enough to be neglected within the confidence interval of our data. It is therefore plausible to assume that the run-out time is a multiple of the decay time and the spreading process is controlled by a single time. We however note that a weak dependence on the energy E'_{x0} is consistent with the fact that the whole available energy at the beginning of the second phase is not dissipated in the spreading process (calculated from the position of the tip of the pile) since the pile keeps deforming by the movements of the particles at the free surface even when the tip comes to rest. This can explain the small difference between the two exponents as observed here.

4.2 Granular column collapse



(a) Evolution of normalised horizontal kinetic energy with time



(b) Evolution of normalised vertical kinetic energy with time

Figure 4.20 Evolution of vertical and horizontal kinetic energy with time

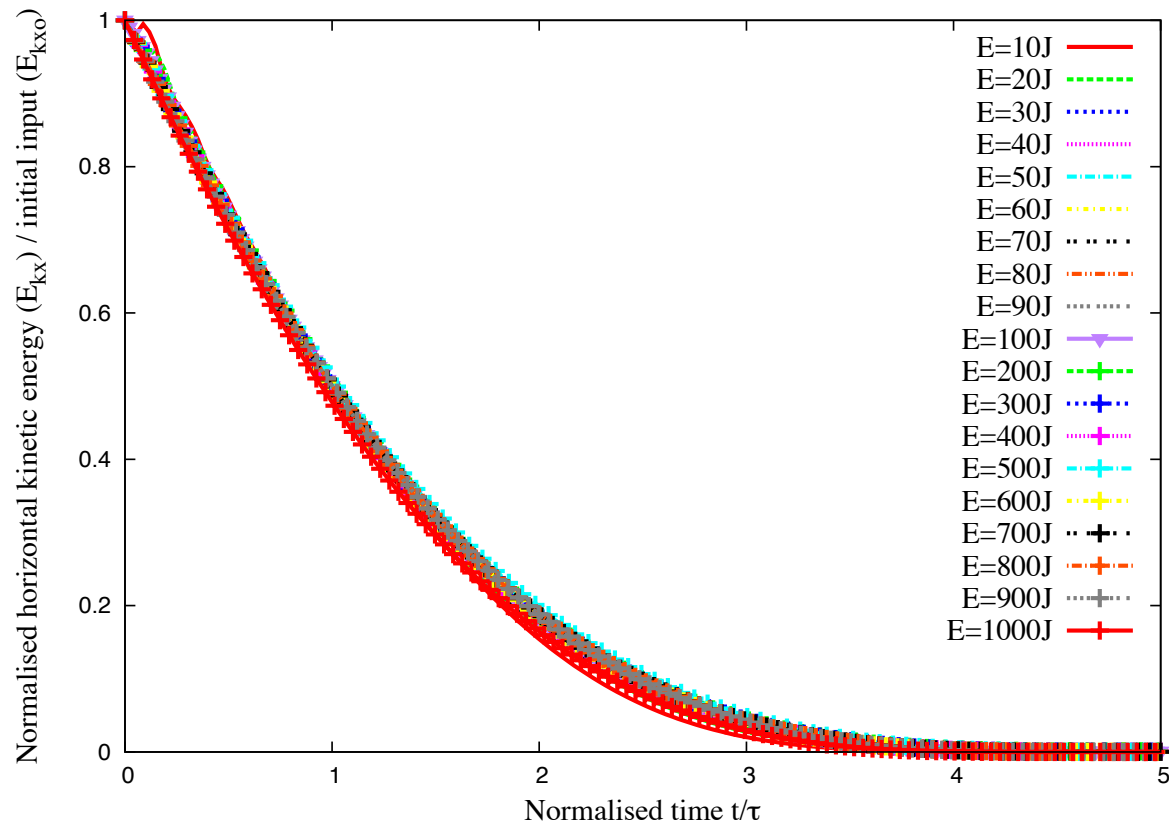


Figure 4.21 Evolution of kinetic energy in the x component of the velocity field normalized by the available kinetic energy at the end of the transient as a function of normalized time.

4.2 Granular column collapse

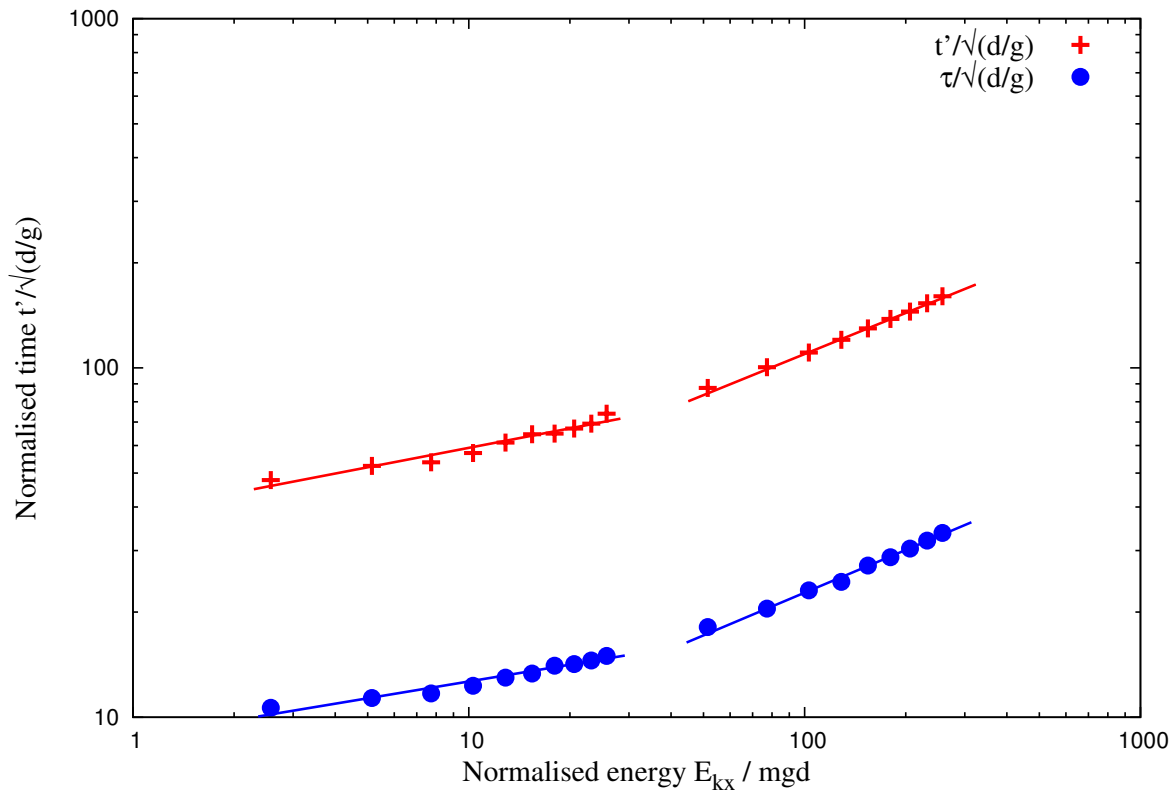
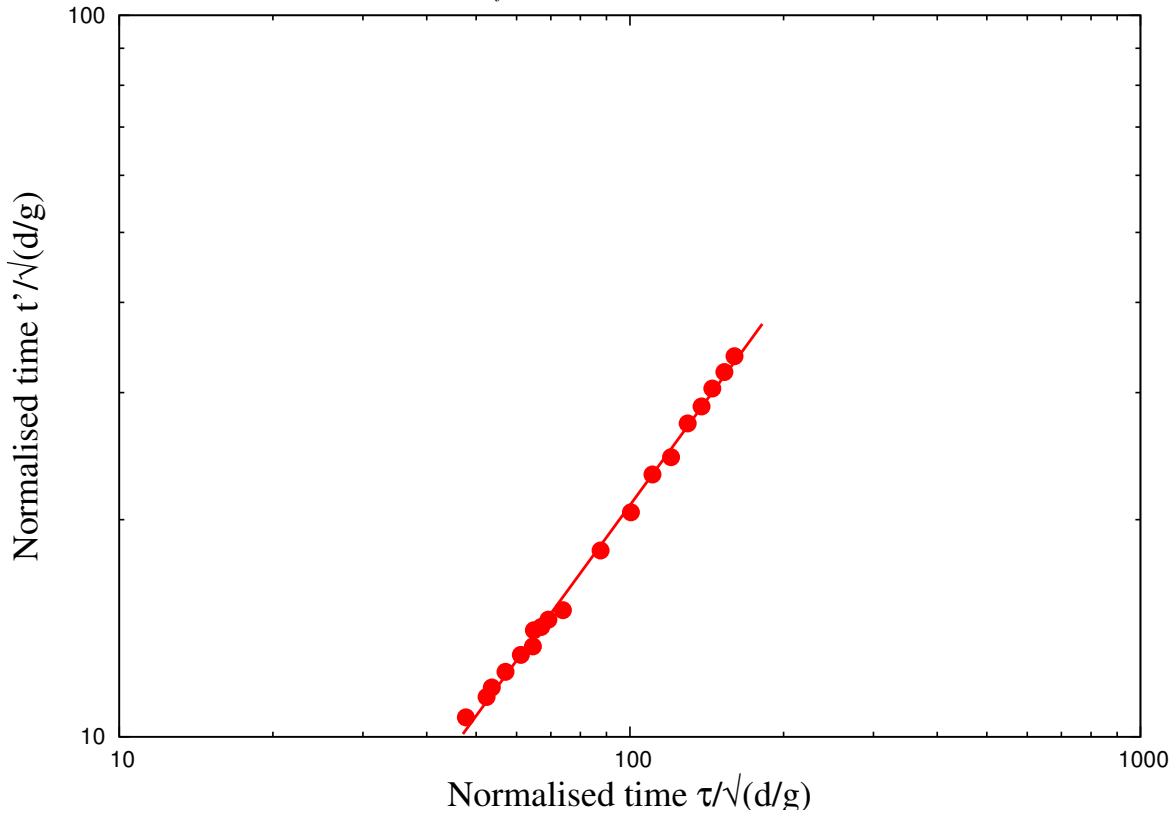
(a) Power law evolution of t'_f and τ as a function of kinetic energy E_{kx0} .(b) Linear relationship between decay time and run-out time after the transient as a function of the normalised kinetic energy E_{kx0} .

Figure 4.22 Decay time and run-out time as a function of the normalised kinetic energy E_{kx0} .

4.2.8 Effect of friction

The run-out distance and time and the dissipation of kinetic energy are controlled by the input energy and collective dynamics of the whole pile, as it was analyzed in the previous sections. But they are expected to depend also on the friction. We performed a series of simulations with different values of base friction. The results are shown in Fig. ?? for the profiles of the pile and evolution of the kinetic energy in time. We see no difference in the results for different values of $e_n = e_t$. This is a consequence of the fact that, even at large input energies, the pile remains in a dense state so that multiple collisions inside the pile occur at small time scales compared to the deformation time. When the restitution coefficients are increased, more collisions occur during a longer time interval but the overall energy dissipation rate by collisions remains the same. This effect is a seminal example of collective effects which erase the influence of local parameters at the macroscopic scale. In contrast with the restitution coefficients, however, the effect of the friction coefficient is quite important for the run-out, as observed in Fig. ?? for both the energy decay and geometrical profile of the pile. Both the run-out distance and decay time decrease as the friction coefficient is increased. This effect is much more pronounced at low values of the friction coefficient. The run-out time, for example, is reduced by a factor 4 as μ_s is increased from 0.1 to 0.4 while the run-out times and profiles do not change much for $\mu_s = 0.7$. This “saturation effect” was evidenced in a systematic way in simple shear tests and explained by the observation that the dissipation rate may reach a saturation point where the dilation of the granular material and rolling of the particles change in response to the increase of the friction coefficient [Estrada et al. \(2008\)](#).

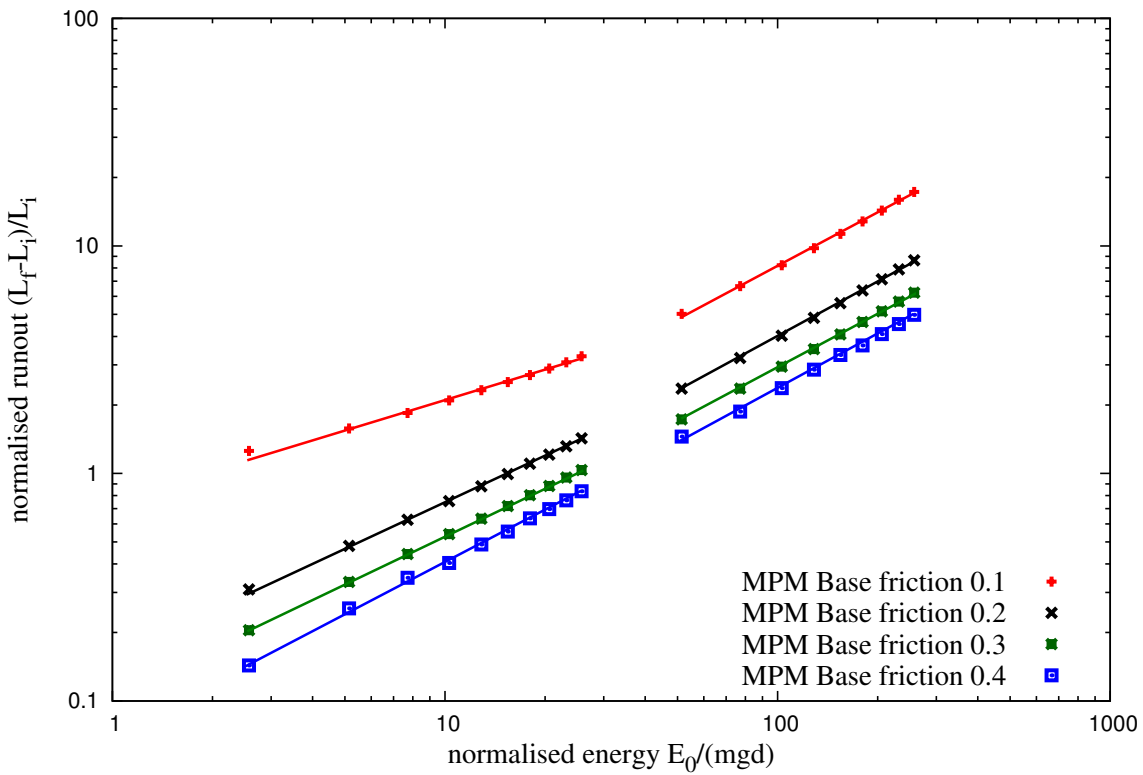
22

23 Mode of dissipation

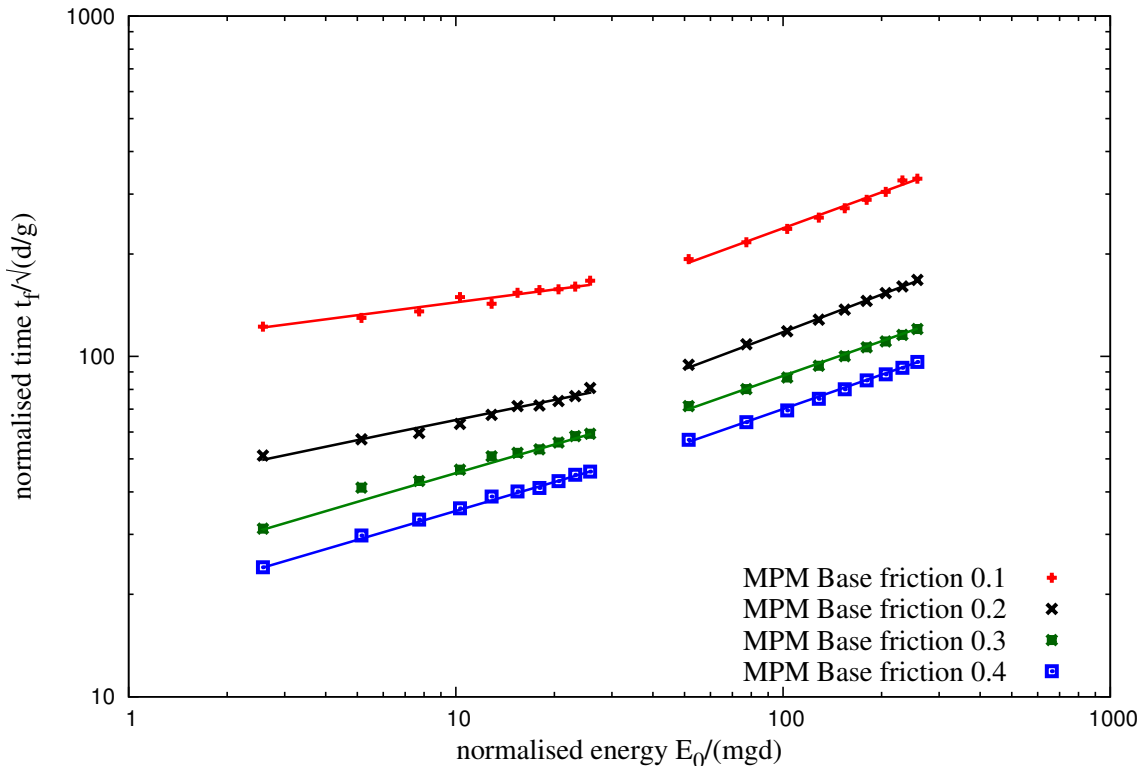
The choice of this geometry was motivated by our main goal to focus on the effect of an input energy on the consecutive dynamics of a granular material. For the range of input energies investigated in this pushing test by means of contact dynamics simulations, we observed a power-law dependence of the run-out distance and time with non-trivial exponents. This is a central result of this work as it reveals that the power-law behaviour is a generic feature of granular dynamics. The values of the exponents are not simple functions of the geometry.

We also evidenced two regimes with different values of the exponents: a low-energy regime and a high-energy regime. The first regime reflects mainly the destabilization of the pile by the quake with a run-out time independent of the input energy whereas the second regime is governed by the spreading dynamics induced by the higher value of the input energy. We showed that the evolution of the pile in this high-energy regime can be described by a

4.2 Granular column collapse

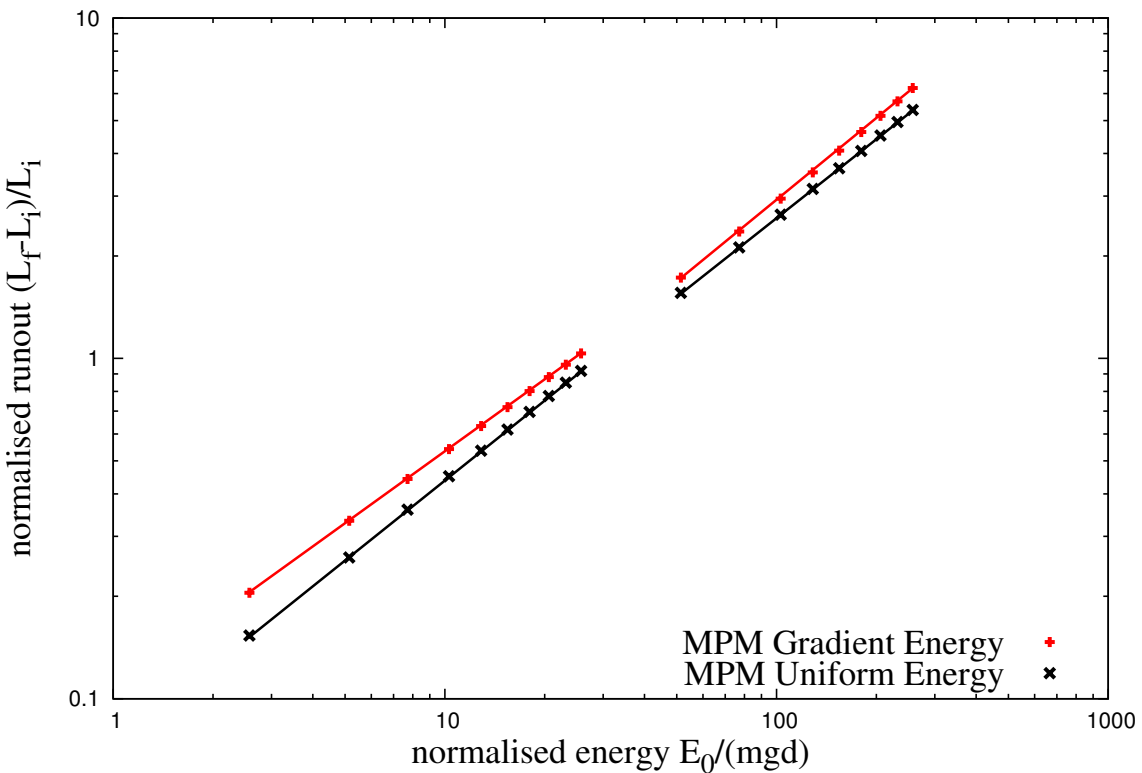


(a) Effect of friction on the run-out distance

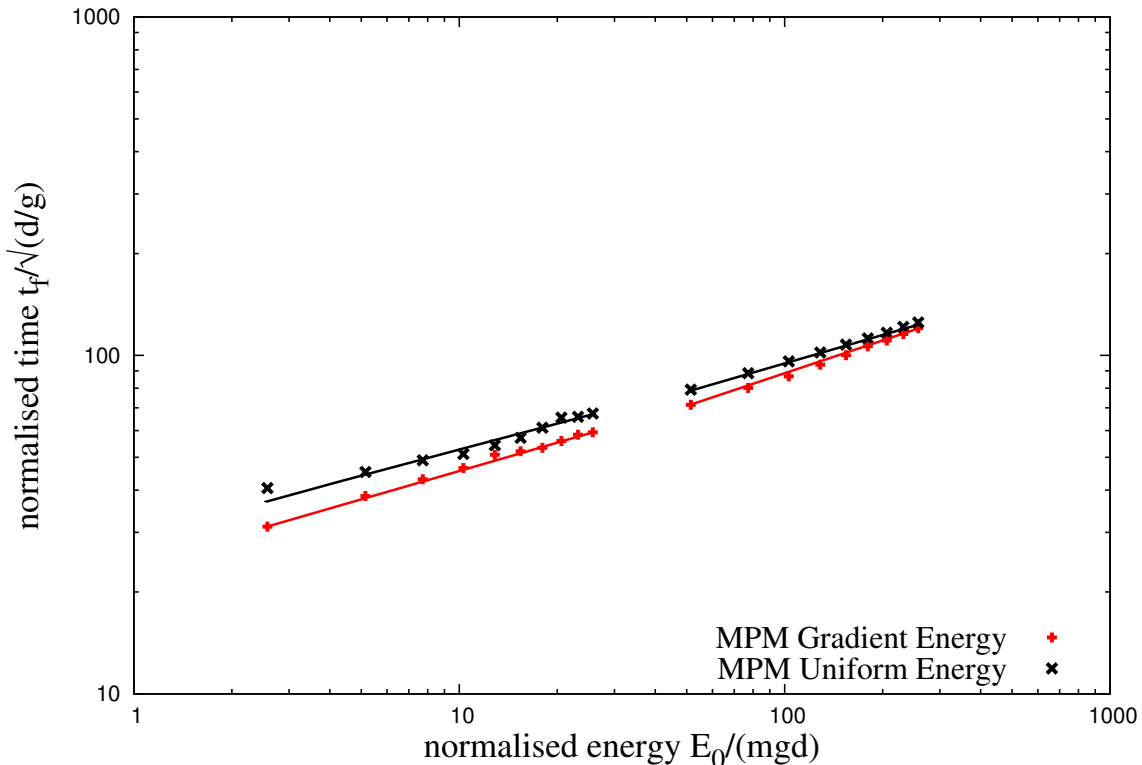


(b) Effect of friction on the duration of run-out.

Figure 4.23 Effect of friction on the run-out behaviour



(a) Run-out distance as a function of normalised input kinetic energy



(b) Duration of run-out as a function of normalised input kinetic energy

Figure 4.24 Effect of input velocity distribution on the run-out behaviour

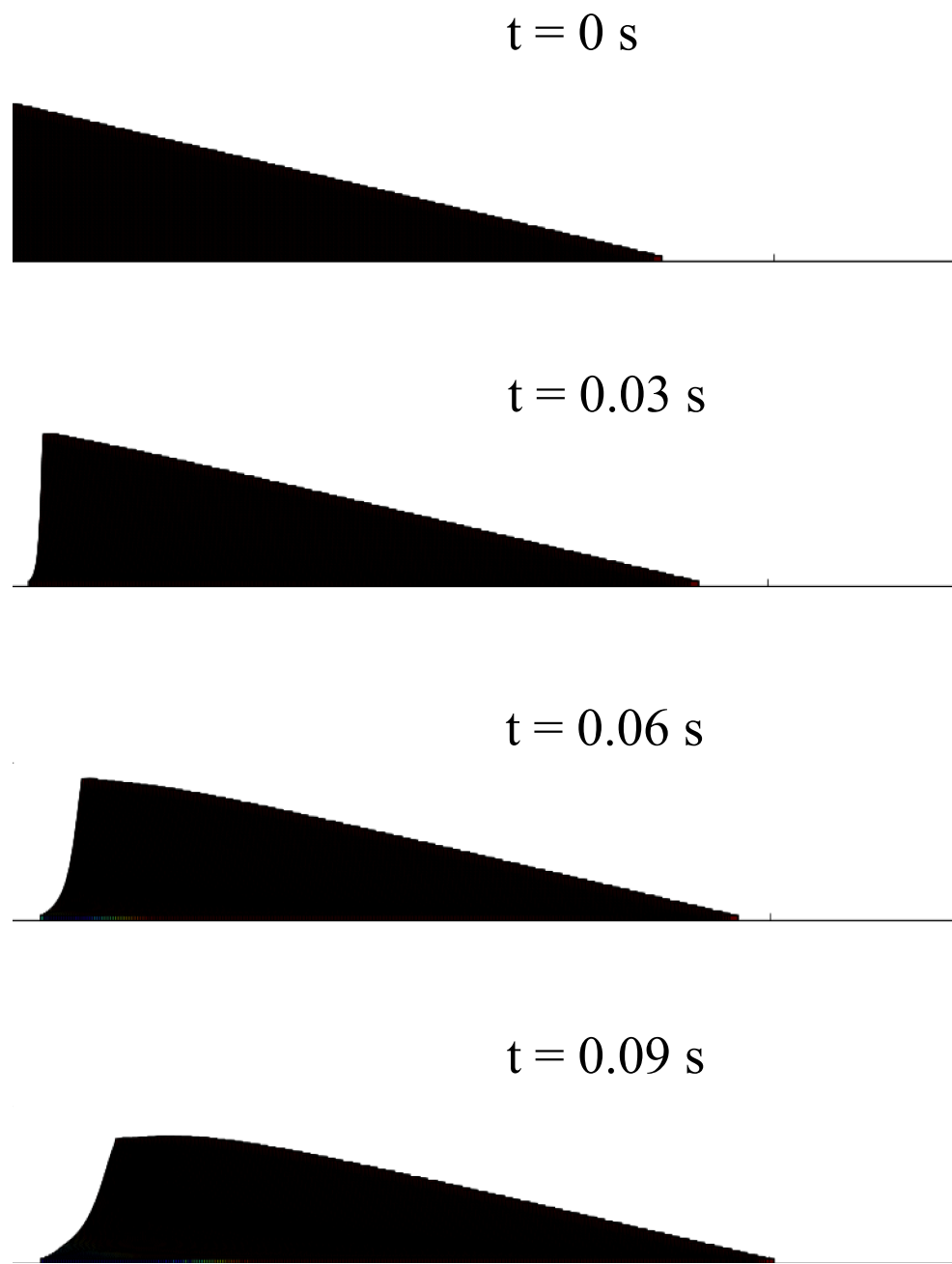


Figure 4.25 Snapshots of MPM simulations of the evolution of granular pile subjected to a gradient impact energy $E_0 = 61 \text{ mgd}$.

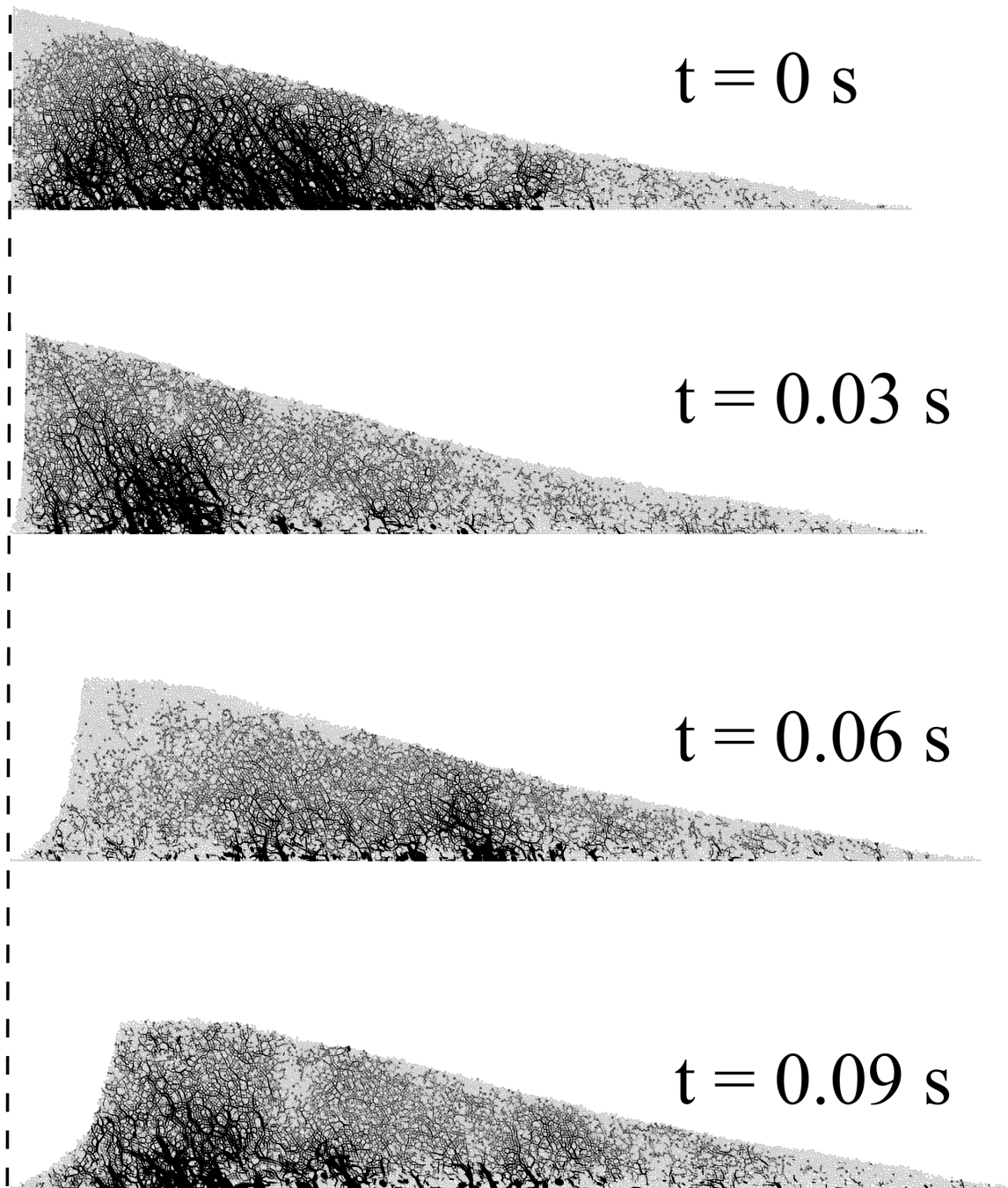


Figure 4.26 Snapshots of DEM simulations of the evolution of granular pile subjected to a gradient impact energy $E_0 = 61 \text{ mgd}$.

characteristic decay time and the energy available at the end of the first stage where the pile is destabilized by the quake.

This work may be pursued along two directions: 1) experimental realization of a similar setup with different modes of energy injection and 2) investigating the effect of various particle shapes or the presence of an ambient fluid. Although numerical simulations are generally reliable with realistic results found in the past studies of steady flows, we believe that the transients are more sensitive situations than steady states and the experiments are necessary for checking the validation of the results suggested by the simulations. Provided a convenient method is used for supplying kinetic energy homogeneously into a pile, our configuration is also interesting for the investigation of the behavior of a pile immersed in a viscous fluid.

4.2.9 Effect of material points

11

4.2.10 Comparison with granular column collapse

12

4.3 Summary

13

Multi-scale simulation of granular column collapse was performed to understand the ability and limitations of continuum models to capture the micro-mechanics of dense granular flows. The run-out behaviour predicted by both continuum and DEM simulations matches for columns with small aspect ratios, where the dissipation is predominantly frictional. However, MPM predicts larger run-out distances for columns with higher aspect ratios. Energy evolution studies using DEM simulations reveal that the run-out behaviour is independent of frictional properties of the granular material and collision predominates the initial free-fall regime. The lack of a collisional energy dissipation mechanism in MPM results in over prediction of run-out distances.

14

15

16

17

18

19

20

21

22

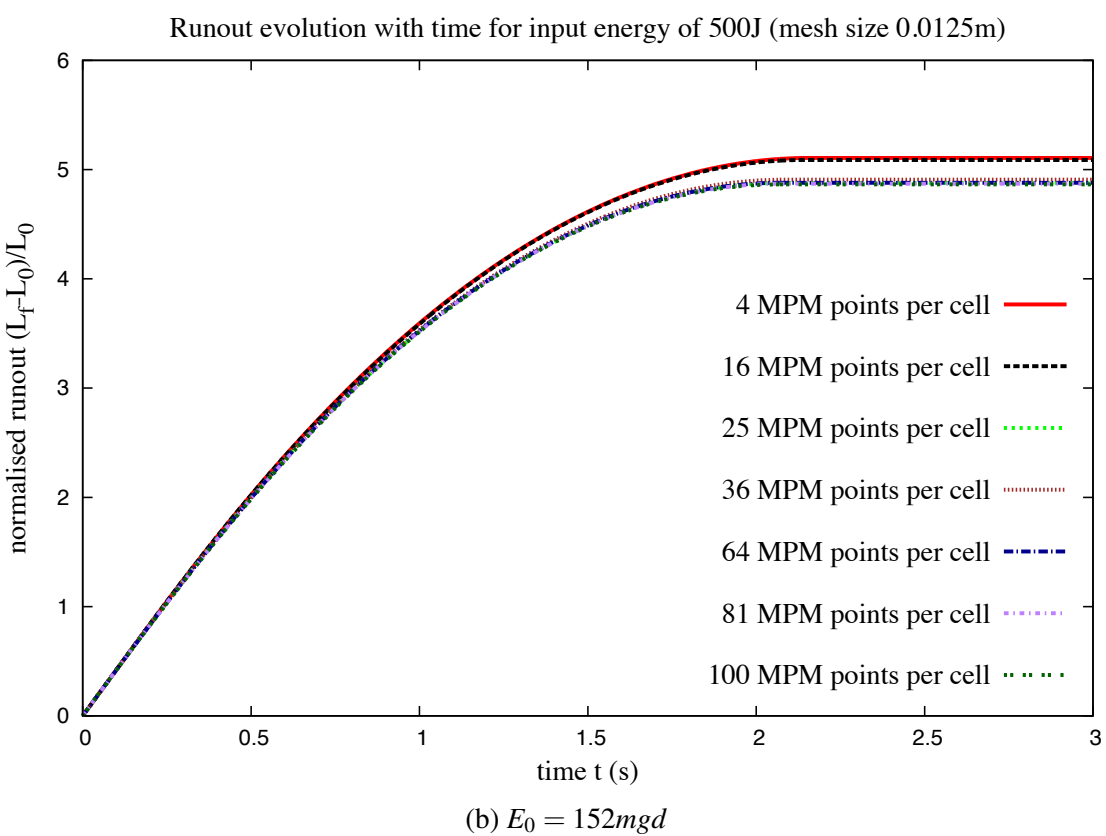
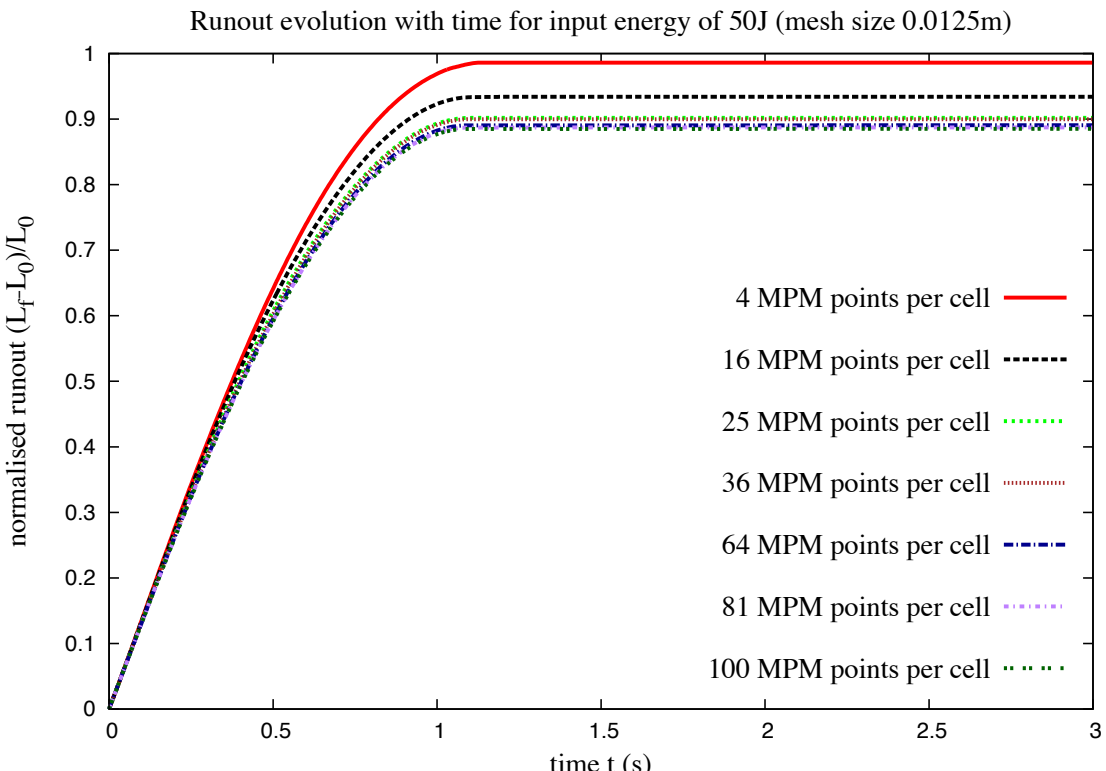


Figure 4.27 Evolution of run-out with time for varying material points per cell.

4.3 Summary

45

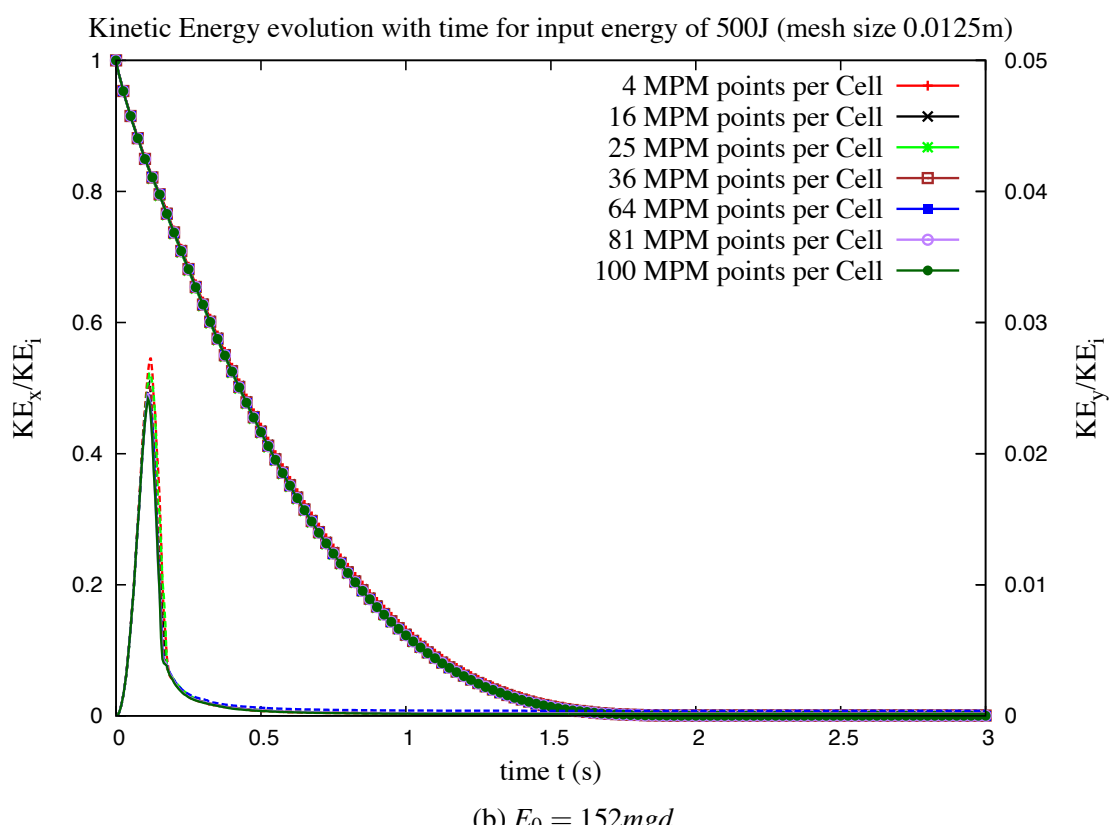
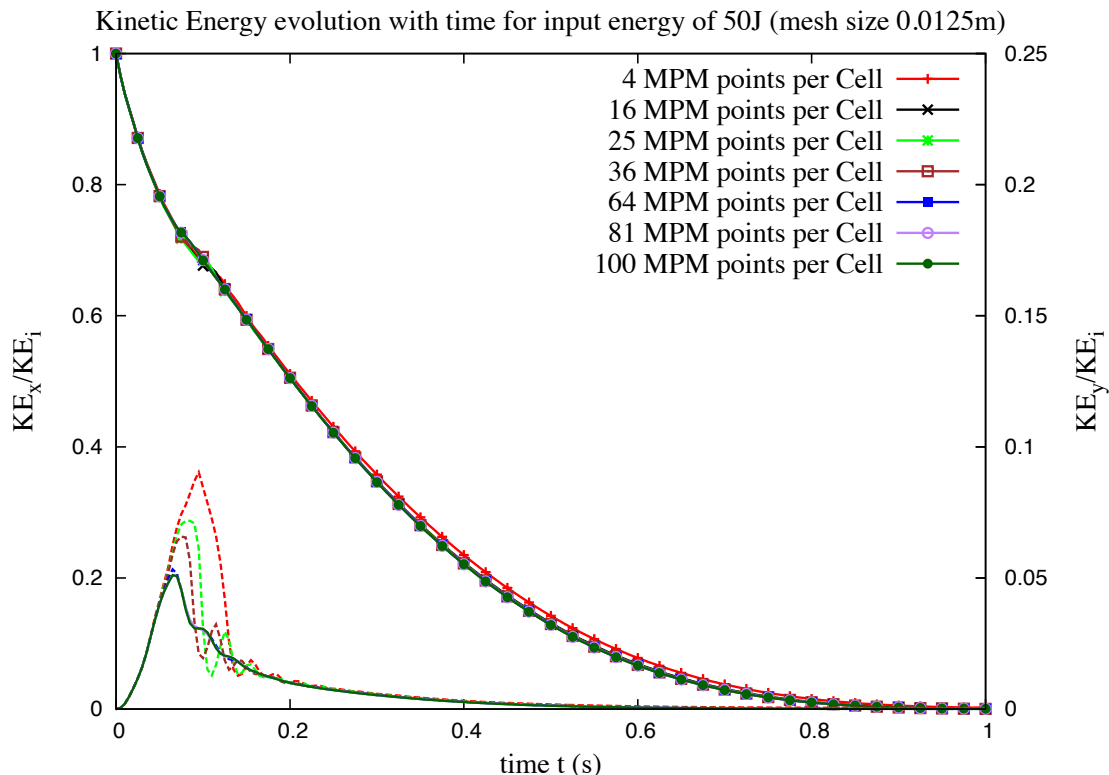


Figure 4.28 Evolution of kinetic with time for varying material points per cell

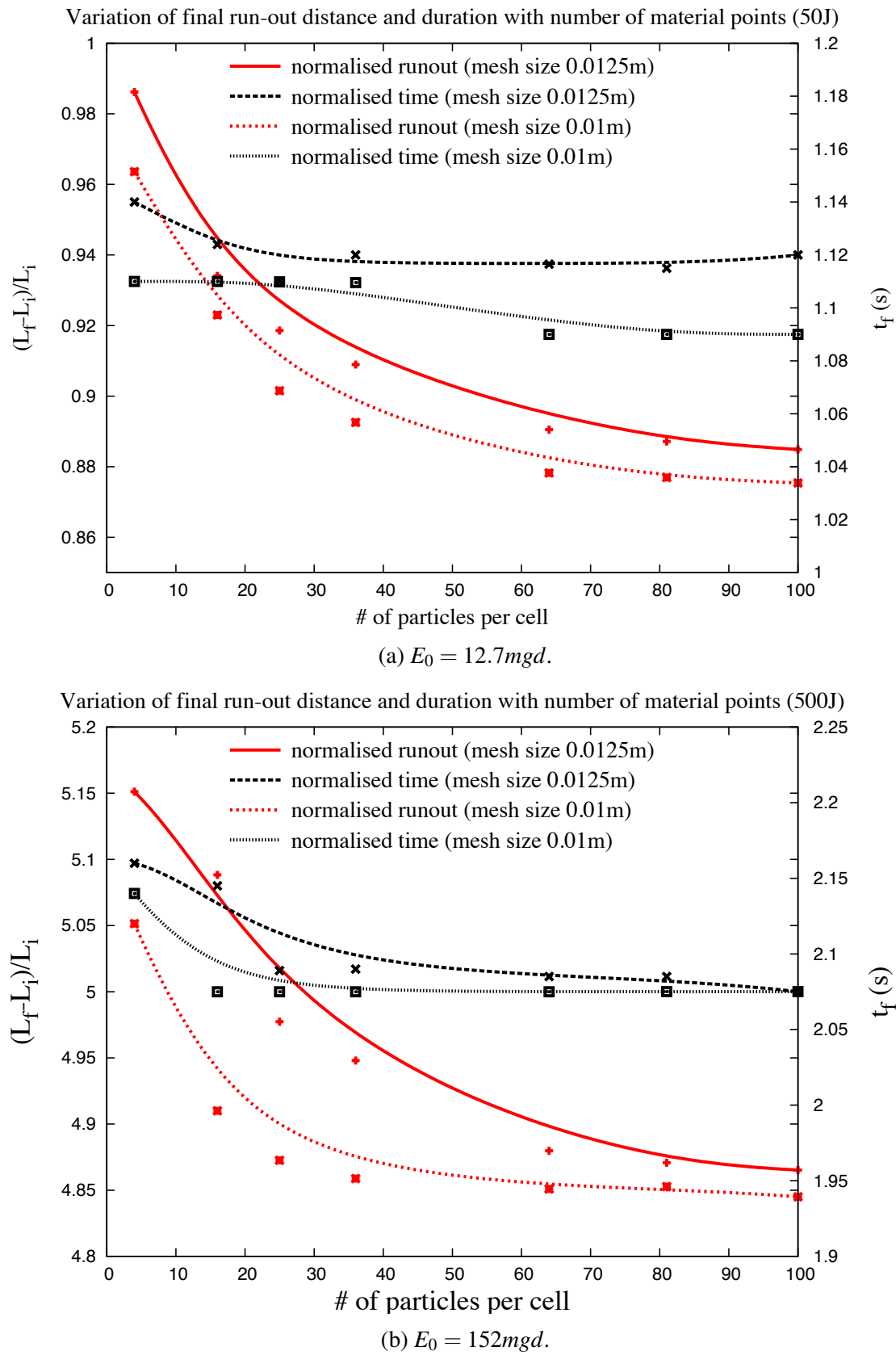


Figure 4.29 Evolution of run-out and duration of flow for varying material points per cell.

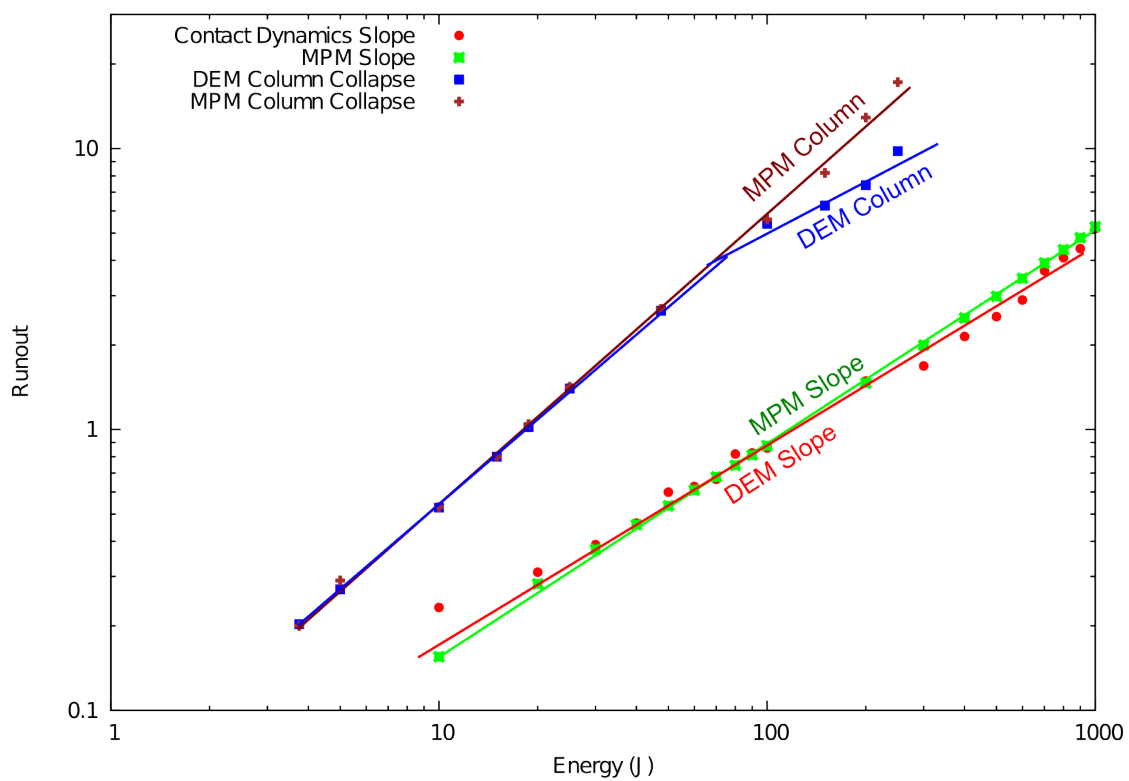


Figure 4.30 Comparison of column collapse with slope subjected to impact loading.

References

- Abe, K., Soga, K., and Bandara, S. (2013). Material Point Method for Coupled Hydromechanical Problems. *Journal of Geotechnical and Geoenvironmental Engineering*, page 04013033. 1
2
3
4
- Balmforth, N. J. and Kerswell, R. R. (2005). Granular collapse in two dimensions. *Journal of Fluid Mechanics*, 538:399–428. 5
6
- Bandara, S. (2013). *Material Point Method to simulate Large Deformation Problems in Fluid-saturated Granular Medium*. PhD thesis, University of Cambridge. 7
8
- Bardenhagen, S. and Kober, E. (2004). The generalized interpolation material point method. *Computer Modeling in Engineering and Sciences*, 5(6):477–496. 9
10
- Cambou, B., Jean, M., and Radjaï, F. (2009). *Micromechanics of granular materials*. Wiley-ISTE. 11
12
- Crosta, G. B., Imposimato, S., and Roddeman, D. (2009). Numerical modeling of 2-D granular step collapse on erodible and nonerodible surface. *J. Geophys. Res.*, 114(F3):F03020. 13
14
- Da Cruz, F., Emam, S., Prochnow, M., Roux, J. N., and Chevoir, F. (2005). Rheophysics of dense granular materials: Discrete simulation of plane shear flows. *Physical Review E - Statistical, Nonlinear, and Soft Matter Physics*, 72(2):1–17. 15
16
17
- Daerr, A. and Douady, S. (1999). Two types of avalanche behaviour in granular media. *Nature*, 399(6733):241–243. 18
19
- Estrada, N., Taboada, A., and Radjai, F. (2008). Shear strength and force transmission in granular media with rolling resistance. *Physical Review E*, 78(2):021301. 20
21
- Girolami, L., Hergault, V., Vinay, G., and Wachs, A. (2012). A three-dimensional discrete-grain model for the simulation of dam-break rectangular collapses: comparison between numerical results and experiments. *Granular Matter*, pages 1–12. 22
23
24
- Guilkey, J., Harman, T., Xia, A., Kashiwa, B., and McMurtry, P. (2003). An Eulerian-Lagrangian approach for large deformation fluid structure interaction problems, Part 1: algorithm development. *Advances in Fluid Mechanics*, 36:143–156. 25
26
27
- Hogg, A. J. (2007). Two-dimensional granular slumps down slopes. *Physics of Fluids*, 19(9):9. 28
- Iverson, R. M. (1997). The physics of debris flows. *Rev. Geophys.*, 35(3):245–296. 29

- ¹ Jean, M. (1999). The non-smooth contact dynamics method. *Computer Methods in Applied Mechanics and Engineering*, 177(3-4):235–257.
- ³ Kerswell, R. (2005). Dam break with Coulomb friction: A model for granular slumping? *Physics of Fluids*, 17:057101.
- ⁵ Lacaze, L. and Kerswell, R. R. (2009). Axisymmetric Granular Collapse: A Transient 3D Flow Test of Viscoplasticity. *Physical Review Letters*, 102(10):108305.
- ⁷ Lajeunesse, E., Mangeney-Castelnau, A., and Vilotte, J. P. (2004). Spreading of a granular mass on a horizontal plane. *Physics of Fluids*, 16(7):2371.
- ⁹ Lajeunesse, E., Monnier, J. B., and Homsy, G. M. (2005). Granular slumping on a horizontal surface. *Physics of Fluids*, 17(10).
- ¹¹ Larrieu, E., Staron, L., and Hinch, E. J. (2006). Raining into shallow water as a description of the collapse of a column of grains. *Journal of Fluid Mechanics*, 554:259–270.
- ¹³ Lo, C. Y., Bolton, M., and Cheng, Y. P. (2009). Discrete element simulation of granular column collapse. In *AIP Conf. Proc. Powders and Grains 2009*, volume 1145 of *6th International Conference on Micromechanics of Granular Media, Powders and Grains 2009*, pages 627–630.
- ¹⁷ Lube, G., Huppert, H. E., Sparks, R. S. J., and Freundt, A. (2005). Collapses of two-dimensional granular columns. *Physical Review E - Statistical, Nonlinear, and Soft Matter Physics*, 72(4):1–10.
- ²⁰ Mitchell, J. K. and Soga, K. (2005). *Fundamentals of soil behavior*. John Wiley & Sons.
- ²¹ Radjai, F. and Dubois, F. (2011). *Discrete-element modeling of granular materials*. ISTE Wiley, London; Hoboken, N.J.
- ²³ Radjai, F. and Richet, V. (2009). Contact dynamics as a nonsmooth discrete element method. *Mechanics of Materials*, 41(6):715–728.
- ²⁵ Rondon, L., Pouliquen, O., and Aussillous, P. (2011). Granular collapse in a fluid: Role of the initial volume fraction. *Physics of Fluids*, 23(7):073301–073301–7.
- ²⁷ Rycroft, C. H., Orpe, A. V., and Kudrolli, A. (2009). Physical test of a particle simulation model in a sheared granular system. *Physical Review E*, 80(3):031305.
- ²⁹ Schaefer, D. G. (1990). Instability and ill-posedness in the deformation of granular materials. *International Journal for Numerical and Analytical Methods in Geomechanics*, 14(4):253–278.
- ³² Staron, L. and Hinch, E. J. (2005). Study of the collapse of granular columns using two-dimensional discrete-grain simulation. *Journal of Fluid Mechanics*, 545:1–27.
- ³⁴ Staron, L. and Hinch, E. J. (2006). The spreading of a granular mass: role of grain properties and initial conditions. *Granular Matter*, 9(3-4):205–217.
- ³⁶ Staron, L. and Hinch, E. J. (2007). The spreading of a granular mass: Role of grain properties and initial conditions. *Granular Matter*, 9(3-4):205–217.

- Staron, L., Radjai, F., and Villette, J. P. (2005). Multi-scale analysis of the stress state in
a granular slope in transition to failure. *The European physical journal. E, Soft matter*,
18(3):311–20.
1
2
3
- Staron, L., Radjai, F., and Villette, J.-P. (2006). Granular micro-structure and avalanche
precursors. *Journal of Statistical Mechanics: Theory and Experiment*, 2006(07):P07014–
P07014.
4
5
6
- Topin, V., Monerie, Y., Perales, F., and Radjaï, F. (2012). Collapse Dynamics and Runout of
Dense Granular Materials in a Fluid. *Physical Review Letters*, 109(18):188001.
7
8
- Utili, S., Zhao, T., and Housby, G. (2014). 3D DEM investigation of granular column collapse:
Evaluation of debris motion and its destructive power. *Engineering Geology*.
9
10
- Warnett, J. M., Denissenko, P., Thomas, P. J., Kiraci, E., and Williams, M. A. (2013). Scalings
of axisymmetric granular column collapse. *Granular Matter*, 16(1):115–124.
11
12
- Zenit, R. (2005). Computer simulations of the collapse of a granular column. *Physics of Fluids*,
17(Compendex):031703–1–031703–4.
13
14